

STRAIN LOCALIZATION AND BULK RHEOLOGY VARIATION  
IN PARTIALLY MOLTEN ROCKS: INSIGHT FROM ANALOGUE EXPERIMENTS OF  
POLYPHASE MATERIALS

by

CONRAD KOZIOL

A THESIS SUBMITTED IN PARTIAL FULFILLMENT OF  
THE REQUIREMENTS FOR THE DEGREE OF

BACHELOR OF SCIENCE (HONOURS)

in

THE FACULTY OF SCIENCE

(Geophysics)

This thesis conforms to the required standard

.....  
Supervisor

THE UNIVERSITY OF BRITISH COLUMBIA

(Vancouver)

MARCH 2011

© CONRAD KOZIOL, 2011

## ABSTRACT

Results of analogue experiments are analyzed to investigate strain localization and the response of materials with volumes of partial melt between 0-38% to applied pure shear. Partial melt is simulated through lower viscosity inclusions of Vaseline in a homogeneous block of higher viscosity paraffin wax. Samples are deformed at a constant natural strain rate in a pure shear, plane strain deformation rig. Processing of the experiments with Particle Imaging Velocimetry software reveal the development of shear bands, linear regions of concentrated shear strain. Shear bands nucleate on low viscosity inclusions and form networks connecting inclusions at low levels of deformation. Deformation within the analogue model experiments is characterized by the dimensionless shear band length, and is found to decrease as the ratio of stress in the Paraffin wax to the stress in the Vaseline increases. The flow stress of our analogue models decreases non-linearly with increasing volume percentage melt. No substantial decrease in the flow stress was found at melt volumes between 0% and 38% corresponding to the rheologically critical melt percentage (RCMP).

## TABLE OF CONTENTS

|  |      |
|--|------|
| TITLE PAGE.....  | i    |
| ABSTRACT.....  | ii   |
| TABLE OF CONTENTS.....   | iii  |
| LIST OF FIGURES.....   | v    |
| LIST OF TABLES.....  | vii  |
| LIST OF EQUATIONS.....   | viii |
| ACKNOWLEDGEMENTS.....  | ix   |
| INTRODUCTION.....  | 1    |
| BACKGROUND.....  | 2    |
| Polymineralic Rheology.....  | 2    |
| Bulk Rheology.....   | 2    |
| Rheologically Critical Melt Percentage.....                                | 2    |
| Strain Localization.....   | 6    |
| METHODOLOGY.....   | 7    |
| Analogue Experiments.....  | 8    |
| Deformation Rig.....   | 8    |
| Experimental Setup.....  | 10   |
| Experiment Geometry.....   | 10   |
| Analogue Materials.....  | 13   |
| Scaling.....   | 12   |
| Data Analysis.....   | 14   |
| Image processing.....  | 15   |
| RESULTS.....   | 24   |
| Flow Stress.....   | 24   |
| Strain Localization in Images.....   | 26   |
| Boundary effects and strain localization on low viscosity inclusions ..... | 27   |
| Shear bands .....  | 29   |
| Deformation .....  | 35   |
| DISCUSSION.....  | 38   |
| Implications for Rheology.....   | 38   |

|   |    |
|---|----|
| Critical Melt Fractions and the Role of Impermeability..... | 39 |
| Strain Localization: Comparison with Previous Work.....     | 40 |
| Shear Band Evolution.....                                   | 40 |
| Deformation.....  | 41 |
| Complications .....   | 41 |
| Analogue Materials.....                                     | 41 |
| Boundary Effects.....                                       | 42 |
| Inclusion Shape and Distribution.....                       | 42 |
| Experimental Approach.....                                  | 42 |
| CONCLUSIONS.....  | 43 |
| REFERENCES CITED.....                                       | 44 |

## LIST OF FIGURES

|   |    |
|---|----|
| Figure 1. Compiled data from rock mechanics experiments investigating the existence of the RCMP .....             | 4  |
| Figure 2. Illustration of the processes of partial melting and magma crystallization .....                        | 5  |
| Figure 3. Schematic illustration of the deformation rig .....   | 9  |
| Figure 4. Illustration of the main geometrical characteristics of the analogue models .....                       | 11 |
| Figure 5. Schematic illustration of Vaseline inclusions in XZ plane.....  | 11 |
| Figure 6. Photograph of Run 88 at 31.7% shortening.....   | 15 |
| Figure 7. Image of the undeformed model in Run 88 placed on a white background.....                               | 16 |
| Figure 8. Image of markings used to align the images.....   | 17 |
| Figure 9a. Run88 at approximately 2% shortening before alignment.....   | 17 |
| Figure 9b. Run88 at approximately 2% shortening before alignment.....   | 17 |
| Figure 10a. Surface of the analogue model Run88 at 32% shortening .....   | 18 |
| Figure 10b. Surface of the analogue model Run88 at 32% shortening processed to show incremental shear strain..... | 18 |
| Figure 10c. Surface of the analogue model Run88 at 32% shortening processed to show cumulative shear strain ..... | 19 |
| Figure 11a. Strain calculations in Run88 viewed in red-green channels.....  | 21 |
| Figure 11b. Strain calculations in Run88 viewed in red-blue channels.....   | 21 |
| Figure 11c. Strain calculations in Run88 viewed in green-blue channels.....                                       | 21 |
| Figure 11d. Strain calculations in Run88 viewed in the red color channel.....                                     | 21 |
| Figure 11e. Strain calculations in Run88 viewed in the green color channel.....                                   | 21 |
| Figure 11f. Strain calculations in Run88 viewed in the blue color channel.....                                    | 21 |
| Figure 12a. Cumulative strain in Run88 at 32% shortening in RGB .....   | 22 |
| Figure 12b. Cumulative strain in Run88 at 32% shortening in blue and green channels .....                         | 22 |
| Figure 13. Transition zone between high strain and low strain .....   | 23 |
| Figure 14. Measuring shear bands using the ruler tool in Matlab .....   | 24 |
| Figure 15. Stress-strain curves plotted for eight analogue model experiments .....                                | 25 |
| Figure 16. Plot of flow stress against volume percentage melt for ten analogue model experiments.....             | 26 |
| Figure 17a. Strain distribution of Run 64 at 26% shortening.....  | 27 |

|   |    |
|---|----|
| Figure 17b. Strain distribution of Run 88 at 26% shortening.....  | 27 |
| Figure 17c. Strain distribution of Run 98 at 26% shortening.....  | 27 |
| Figure 18. Image of Run 98 at 32% shortening comparing strain distribution and Vaseline inclusions locations.....     | 29 |
| Figure 19a. Image of Run 84 showing initiation of shear band network.....   | 30 |
| Figure 19b. Image of Run 88 showing initiation of shear band network.....   | 30 |
| Figure 19b. Image of Run 90 showing initiation of shear band network.....   | 31 |
| Figure 19d. Image of Run 96 showing initiation of shear band network.....   | 31 |
| Figure 19e. Image of Run 98 showing initiation of shear band network.....   | 31 |
| Figure 20a. Strain distribution of Run 84 at 19.5% shortening.....  | 33 |
| Figure 20b. Strain distribution of Run 88 at 19.5% shortening.....  | 33 |
| Figure 20c. Strain distribution of Run 90 at 19.5% shortening.....  | 33 |
| Figure 20d. Strain distribution of Run 96 at 19.5% shortening.....  | 33 |
| Figure 20e. Strain distribution of Run 98 at 32% shortening.....  | 33 |
| Figure 21a. Strain distribution of Run 84 at 32% shortening.....  | 34 |
| Figure 21b. Strain distribution of Run 88 at 32% shortening.....  | 34 |
| Figure 21c. Strain distribution of Run 90 at 32% shortening.....  | 35 |
| Figure 21d. Strain distribution of Run 96 at 32% shortening.....  | 35 |
| Figure 21e. Strain distribution of Run 98 at 32% shortening.....  | 35 |
| Figure 22a. Dimensionless lengthscale of shear bands vs ratio of viscous forces at shear band network initiation..... | 36 |
| Figure 22b. Dimensionless lengthscale of shear bands vs ratio of viscous forces at 19.5% shortening.....              | 36 |
| Figure 22c. Dimensionless lengthscale of shear bands vs ratio of viscous forces at 32% shortening.....                | 37 |

## LIST OF TABLES

|   |    |
|---|----|
| Table 1. List of analogue model experiments.....  | 12 |
| Table 2. Volume percent melt of analogue models and their corresponding flow stress ..... | 25 |
| Table 3. Percentage shortening interval at which a shear band networks appeared.....      | 32 |

## LIST OF EQUATIONS

|  |    |
|--|----|
| Equation 1. Natural Strain.....  | 8  |
| Equation 2. Natural Strain Rate .....  | 9  |
| Equation 3. Model length at time step $\Delta t$ .....                           | 9  |
| Equation 4. Force in the high viscosity matrix.....                              | 13 |
| Equation 5. Force in the low viscosity inclusions.....                           | 13 |
| Equation 6. Viscosity of the matrix.....   | 13 |
| Equation 7. Ratio of the force in the matrix to the force in the inclusions..... | 14 |
| Equation 8. Constant used in Equation 7.....                                     | 14 |
| Equation 9. Dimensionless shear band length.....                                 | 14 |
| Equation 10. Empirical fit of flow stress data.....                              | 26 |

## ACKNOWLEDGEMENTS

Djordje Grujic

Mark Jellinek

Mary Lou Bevier

Geology Graduate Students of Dalhousie University

## 1. Introduction

Strain localization in deformed rocks is observed on scales from kilometer, outcrop, to individual grains (e.g., Ramsay, 1980; Handy, 1990; Grujic, 1998). In many natural settings, strain localization is influenced by the presence of partial melt. The presence of melt affects both the bulk rock rheology and the pattern of developing shear zones. Characterizing the influence of partial melt the pattern and development of strain localization in natural rocks would enable better modelling of the melt transport and rheological properties of deforming regions within the earth.

Increasing volume percentages of partial melt decrease the viscosity of rocks (Takeda and Obata, 2003). Whether viscosity decreases gradually as the fraction of melt increases, or whether there is a critical fraction of melt at which the viscosity rapidly decreases is debated. (see Takeda and Obata, 2003) The rheologically critical melt percentage (RCMP) (Arzi, 1978) is the melt fraction at which the viscosity of rocks is significantly reduced. Quantifying the RCMP and determining the rheological behavior of partially molten rocks would contribute to our understanding of the lower crust and the origin of granitic magmas. (Takeda and Obata, 2003)

Since partial melting and shear zone development are observed in the field to be associated in high grade metamorphic terrains, shear zone development can be observed indirectly in natural rocks (Means, 1995). In field examples, leucosomes (crystallized felsic melts) are found in shear zones (e.g., Hollister and Crawford, 1986; Davidson et al., 1994; Brown et al., 1995). Whereas directly observing melt segregation and shear zone development is not possible, leucosomes provide a snapshot of deformation at a particular stage. Rock mechanics experiments (Holtman et al., 2003; Rosenberg and Handy, 2005; Rutter et al., 2006) mathematical modelling (Stevenson, 1989, Spiegelman, 1993; Butler, 2010), and scaled modelling using analogue materials (Grujic and Mancktelow, 1998; Rosenberg and Handy, 2000; Barruad, 2001) model strain localization and investigate the effects of partial melt on rheology over large strains.

My thesis is to analyze the results of analogue model experiments simulating natural rocks containing partial melt conducted by Dr. Grujic. The experimental data is analyzed to

determine the influence of partial melt on the bulk rheology of the models and the influence of partial melt on strain localization. Flow stresses of the models are determined from stress-strain curves and their dependence on volume percentage partial melt is investigated. Low viscosity inclusions simulating partial melt are found to nucleate shear bands that connect into networks at low stages of deformation. The evolution of the shear band networks with progressive shortening is described and related to stress-strain curves. Deformation within the experiments is characterized and found to be dependent on the ratio of forces in the high viscosity matrix to low viscosity partial melt.

My thesis is organized into six sections. Section 1 introduces the topic and relevance my thesis. Section 2 describes previous work on the subject. Section 3 details the methodology of the experiments and my analysis. Section 4 describes the results of my analysis. Section 5 discusses the results. Section 6 draws conclusions from my analysis.

## **2. Background**

### 2.1 Polymineralic Rheology

#### *2.1.1 Bulk Rheology*

Polymineralic rocks have either framework-supported or matrix-supported rheologies (Handy, 1990). Framework-supported rheologies have a load bearing framework of strong minerals with weak minerals in interstitial spaces, whereas matrix supported rheologies are dominated by the weaker phase with inclusions of higher viscosity phases forming boudins or clasts within the surrounding matrix. Weak mineral shape and distribution influences the rheology of load bearing frameworks, and with increasing aspect ratio of the interstitial spaces stress concentration increases in the strong phase (Handy 1990). The boundary between the two rheologies is the RCMP (Handy 1990).

Handy (1990) reports viscosity contrasts of one or two orders of magnitudes between melt and solid phase. Though weak inclusions are generally thought to decrease rock viscosity, Handy (1990) suggests that at proportions of less than 0.1, weak phase within a framework supported matrix increases the viscosity of the aggregate beyond that of the most viscous constituent material. Rocks with a framework-supported rheology are thought to

comprise a minor part of the lithosphere, and generally take the form of mafic lower crustal/upper mantle rock (Handy 1990).

### *2.1.2 Rheologically Critical Melt Percentage*

Arzi (1978) defines the RCMP as the melt fraction at which a significant drop in the viscosity of rocks is observed. The RCMP is based on modelling the viscosity of partially molten materials as a suspension of solid spheres in a fluid by Einstein (1906, 1911) who formulated the model for the rheology of a dilute suspension of spheres in a fluid with negligible interaction of the particles. Roscoe (1952) extended this formulation to dense suspensions by assuming an idealized packing configuration at higher densities. Using this formulation, at particle fractions approaching 74% (26% fluid or 'partial melt'), the ratio between the viscosity of the bulk fluid with suspended particles to the viscosity of the pure fluid increases rapidly to become infinite (Takeda and Obata, 2003). Applying Roscoe's (1952) model to experiments investigating the effect of varying melt fraction on the viscosity of partially melted granite, Arzi (1978) explained the drastic viscosity drop he saw between 10% and 30% of partial melt with the RCMP. The RCMP is interpreted as the transition between a framework structure of particles to a liquid state with suspended particles (Arzi, 1978). The drop in viscosity was thought to occur at the RCMP due to the fundamental change in the structure of the partially molten rock.

Subsequent experimental results on partially molten granite yielded results both favorable and unfavorable to the concept of RCMP (e.g., Van der Molen and Paterson, 1979; Rushmer, 1995; Rutter and Neumann, 1995) (Figure 1). Further theoretical work investigating the physical processes of partial melt influencing viscosity provided more detailed formulations of the RCMP. In crystallizing magmas, the rock melt situates itself in pockets within a solid framework, whereas during partial melting, rock melt forms melt films along grain boundaries. For similar melt fractions, there is more melt interconnection during partial melting than in crystallization. Vigneresse et al. (1996) proposed that the RCMP occurs between the melt fraction of 8%-25% during the transition from liquid to solid in crystallizing magmas and between the melt fraction of 25%-45% during the transition from solid to liquid in partially molten rocks (Figure 2).

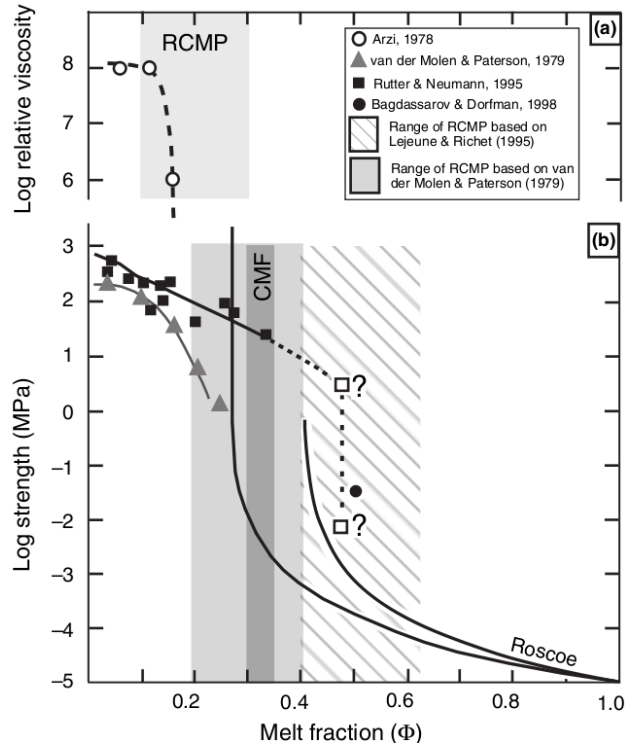


**Figure 1:** Rosenberg and Handy's (2005) plot of rock strength as a function of melt fraction on a logarithmic plot. Data is compiled from literature. (a) Plot of data from Arzi (1978), with the predicted interval of melt fractions corresponding to the RCMP highlighted in light gray. Relative viscosity (sample viscosity / melt viscosity) was used as a measure of strength. (b) Data from experiments performed by van der Molen & Patterson (1979), and Rutter & Neumann (1995) with rock strength measured in MPa. The interval of melt fractions corresponding to the RCMP constrained by the experiments of van der Molen & Patterson (1979) is shown in light grey, and dashed lines for the interval predicted by Lejeune & Richet (1995). The relationship between aggregate strength and melt fraction predicted by the theoretical formulation of Roscoe (1952) is plotted using the parameters of both Lejeune & Richet (1995) (right curve) and Arzi (1978) (left curve). The volume percent melt at which rock strength decreases most rapidly is known as the Critical Melt Fraction (CMF). The CMF from van der Molen & Paterson (1979) is highlighted in dark grey.

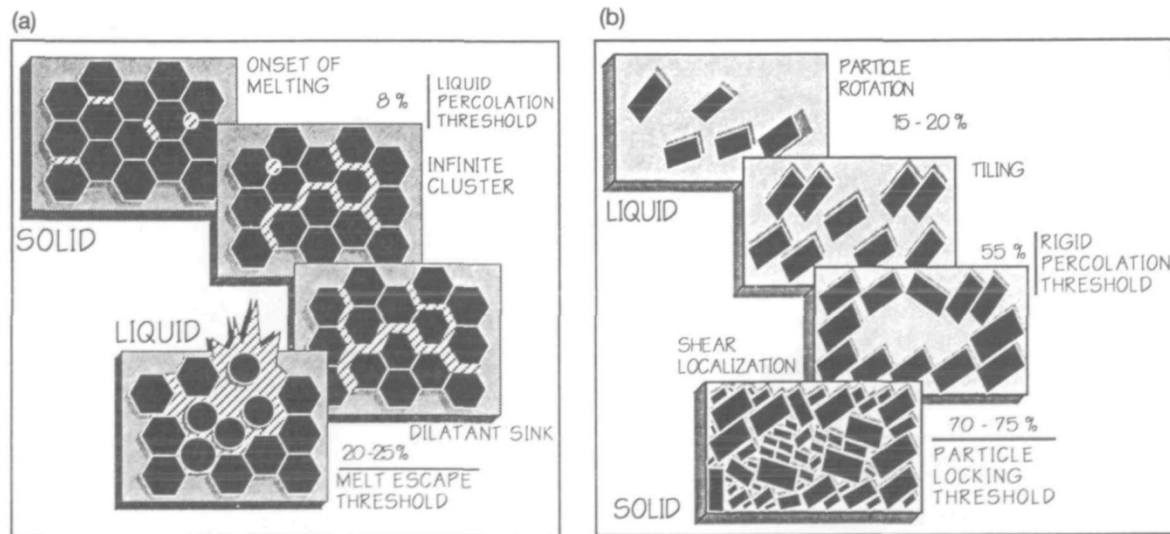


**Figure 2:** Illustration of the processes of partial melting and magma crystallization (Vigneresse, 1996). a) Schematic illustration of the rheological transition from solid to liquid during partial melting. The RCMP is proposed to be in the interval of 8% to 20-25% volume melt, which are known as the Liquid Percolation Threshold (LPT) and the Melt Escape Threshold (MET) respectively. The LPT is characterized by a continuous melt film along grain boundary connecting pockets of melt, while the MET is characterized by the segregation and transport of magma, with the ability to transport the solid phase. b) The transition from melt to solid during magma crystallization is a different process than partial melting, and the RCMP occurs over a different range of melt volume percentage. The RCMP is proposed by Vigneresse (1996) to occur within the range of 55% to 70-75% melt volume. The onset of this range is known as the Rigid Percolation Threshold, and is characterized by formations of particles sustaining stress while accommodating flow of the liquid phase. The Particle Locking Threshold, the end of the range where the RCMP occurs, is reached when particles form a locked framework.

In a reanalysis of the data of van der Molen and Paterson (1979) Takeda and Obata (2003) found a linear relationship between partial melt and rock viscosity. Rosenberg and Handy (2005) conclude the RCMP exists at a melt fraction of 35% after a reanalysis of available data sets. However, even though the drop in aggregate viscosity at 35% melt volume may be greater than five orders of magnitude, in absolute value it is less than 1 MPa. Because the viscosity reduction at the RCMP was much smaller than previously thought, Rosenberg and Handy (2005) renamed the RCMP the solid to liquid transition (SLT). Furthermore, their interpretation of previous experiments suggests that the aggregate viscosity of rocks is most dependent on partial melt at melt volumes of 0% to 7%, finding

that experiments experienced a ~750 Mpa drop in viscosity from the melt interval of 0% to 7%. Rosenberg and Handy (2005) termed the 7% melt volume the melt connectivity transition (MCT). Rosenberg and Handy (2005) suggest that melt interconnectivity is the mechanism behind the strength drop below the MCT. In the melt volume interval between 0% melt volume and the MCT, additional melt greatly increases the proportion of grain boundaries containing melt. At melt fractions greater than the MCT, the number of grain boundaries containing melt is not significantly increased by additional melt; instead the melt films at grain boundaries become thicker. The significant increase in the proportion of boundaries containing melt below the MCT is the reason significant weakening is seen (Rosenberg and Handy, 2005). Melt fractions of the SLT and MLT are predicted to be independent of the melting or crystallizing state of the rock, since melt distribution in rocks with melt volume greater than 40% is determined by the orientation and magnitude of the applied stress and finite strain (Rosenberg and Handy, 2005).

## 2.2 Strain Localization

Under a given applied differential stress, strain is concentrated in low viscosity material relative to high viscosity material. Previous analogue (Grujic and Mancktelow, 1998) and numerical experiments (Mancktelow, 2001) show that shear zones nucleate on weak inclusions and connect to form a through-going anastomosing pattern of shear zones. In pure shear experiments, concentrated zones of high shear strain enclosed areas experiencing near coaxial strain (Grujic and Mancktelow, 1998). Numerical modelling by Mancktelow (2001) investigates parameters influencing shear zone development and the geometry of strain localization on low viscosity inclusions using both pure shear and simple shear boundary conditions. In the models, conjugate shear zones initiate at 90° to each other centred on the low viscosity inclusions, rotating and stretching towards the bulk  $X$  direction with increasing bulk deformation. In Mancktelow's (2001) pure shear numerical simulations using initially cylindrical low viscosity inclusions, the pattern of stress and shear bands was symmetrical about the infinitesimal incremental and finite shortening direction. Changing the viscosity contrast between the inclusions and matrix over a range of 2-200 resulted in minimal variations in the outcome of the experiment. Shear bands formed at low levels of

deformation at approximately 45° to the shortening axis. Shear bands enclosed areas of matrix experiencing lower amounts of strain than the shear zones. As the the shear zones rotated during deformation, the matrix also deformed. The maximum difference in strain between shear zone and matrix was approximately 20. This peak value was reached when the shear zones were at an optimal angle for localization of strain within the shear zones, approximately 45° to the shortening axis. After the peak difference in strain between shear zones and matrix was reached, the difference in strain between shear zone and matrix decreased with increasing amounts of deformation (Mancktelow, 2001).

Deformational experiments on synthetic rocks under simple shear showed melt bands emerging and persisting at 15-25° to the plane of shear (Holtzman et al., 2003). Similar results in other experiments led Holtzman et al. (2003) to suggest that this angle interval is not controlled by the matrix but by stress. Theoretical work showed that these angles are the most favorable orientation when considering porosity-weakening and strain-rate-weakening viscosity (Katz et al., 2006).

### **3. Methodology**

Analogue modelling using a high viscosity matrix containing low viscosity inclusions simulating rocks containing partial melt was performed by Dr. Grujic with the following goals:

- To determine if the flow stress of the analogue models decreases linearly as a function of the volume percentage melt, or whether there is a rapid decrease in flow stress of the analogue models over the volume percentage melt in the range of 10-30% corresponding to the RCMP.
- To investigate whether the presence of partial melt would localize strain into shear bands.
- If shear bands form, to determine the percent shortening of the experiments at which shear bands form an interconnected network.
- Qualitatively describe the evolution of shear bands as the analogue models are progressively shortened and relate the evolution of shear bands to the stress-strain

curve of each model.

- Describe the deformation of the analogue model as function of the ratio of force in the high viscosity matrix to the force in the low viscosity inclusions.

Analogue models were constructed and deformed by Dr. Grujic in 1996 at the Department of Earth Sciences, Swiss Federal Institute of Technology Zurich (ETH Zurich). Analogue models were constructed of a high viscosity homogeneous matrix of paraffin wax with lower viscosity Vaseline inclusions simulating pockets of partial melt and deformed under pure shear, plane strain conditions

The applied differential stress to the models and corresponding level of shortening are measured during deformation of the analogue models. These data are used to produce stress-strain curves and determine the flow stress. Above the deformation rig, a high-resolution camera photographs the experiments at regular shortening intervals. Photographs documenting six representative experiments were digitized and processed to show strain in the analogue models using particle imaging velocimetry software. Using the processed images, shear bands are identified, their length measured, and the percent shortening at which shear band networks formed is determined.

### 3.1 Analogue Experiments

#### 3.1.1 Deformation Rig

Analogue models in the deformation rig are enclosed by six plates. (Figure 3) The top and bottom plates are fixed and prevent deformation in the Y-direction (the direction of view of the experiments), resulting in plane strain deformation. The remaining four plates are attached to pistons. Two opposing pistons compress the analogue model (Z bulk strain direction), while the other pair of opposing pistons provide a confining stress (X bulk strain direction). The two pairs of pistons are driven by independent motors controlled by a computer and shorten the model at a constant strain rate, where strain  $\epsilon$ , is the natural or logarithmic strain (Equation 1).

$$\epsilon = \ln\left(\frac{l}{L}\right) \quad (1)$$

where  $l$  is the current length of the model and  $L$  is the original length of the model. The natural strain rate is given by Equation 2.

$$\dot{\epsilon} = \frac{\epsilon}{\Delta t} \quad (2)$$

where  $\Delta t$  is the time step in the experiment. Model length at time step  $\Delta t$  is given by Equation 3.

$$l = L \exp(\dot{\epsilon} \Delta t) \quad (3)$$

Above the deformation rig a high-resolution camera photographs the top surface of the model (in the XZ plane) triggered by a computer at predetermined shortening intervals. The entire deformation rig is thermally insulated and the temperature during the experiments is controlled to within  $\pm 0.1$  °C. Mancktelow (1988a) describes the deformation rig used in the experiments in detail.

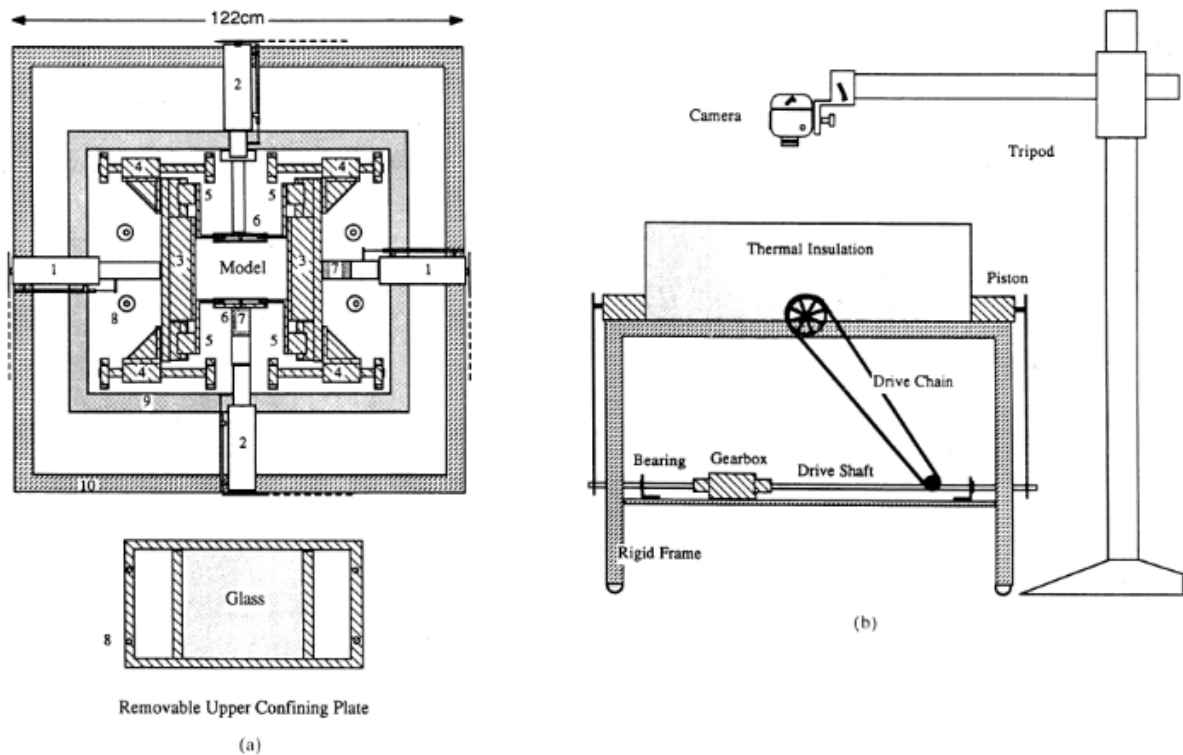


**Figure 3:** Schematic illustration of the deformation rig (Mancktelow, 1988a). (a) Plan view of the plane strain, pure shear machine with the upper confining plate removed. 1: Compression piston with displacement transducer; 2: confining piston with displacement transducer; 3: compression plates faced with 5mm Teflon sheet; 4: linear bearing for the compression plates which run on a stainless steel bar; 5: linear bearing for the side plates.

The runner bar is mounted on the compression plate assembly 3; 6: three-piece side plate assembly. The central section is notched onto the confining piston 2 and remains stationary relative to this piston; 7: force transducer with a range of 0-5000 N; 8: anchoring points for the upper confining plate; 9: thermal insulation 5 cm thick surrounding the whole rig; 10: rigid frame for the rig. (b) Side view of the pure shear rig with the thermal insulation box and camera in place.

### *3.1.2 Experimental Setup*

Blocks of paraffin wax are created to the dimensions of the deformation rig by pouring molten wax into a mold containing aluminum cylinders of the number, distribution, and geometry of the desired Vaseline inclusions. Once cooled, the paraffin wax block is machined to the desired size, the aluminum cylinders carefully removed, and the holes carefully filled with Vaseline using a syringe. The plates of the deformation rig are lubricated and the paraffin wax block is centred inside the plates. The top plate is transparent allowing photographs of the top surface of the analogue model, and a label with the experiment number and date is taped to the top plate. Over a twenty four hour time period, the experiment and deformation rig is heated to a homogeneous temperature of 24°C. Since wax volume has a strong dependence on temperature, the paraffin block of wax expands slightly within the deformation rig. After the wax is homogeneously heated, a 5x5mm grid was painted onto the top of the paraffin wax block for Run 64, Run 84, Run 88, and Run 90. At the time of experiments, this was the only technique available for monitoring strain (by hand digitizing the grid from each photograph, (i.e., Mancktelow, 1991). Experiments were run to 35-40% shortening at confining stresses of 10-50kPa (Table 1).

### *3.1.3 Experiment Geometry*

Figure 4 illustrates the main geometrical characteristics of analogue models before deformation. Experiment dimensions are: 290mm in length; 130mm in width; 60mm in height. Inclusions of Vaseline are distributed homogeneously in the experiment and have their longest axis parallel to the intermediate bulk strain axis Y, with cross sections in the XZ plane. The inclusion cross sections used are illustrated in Figure 5.

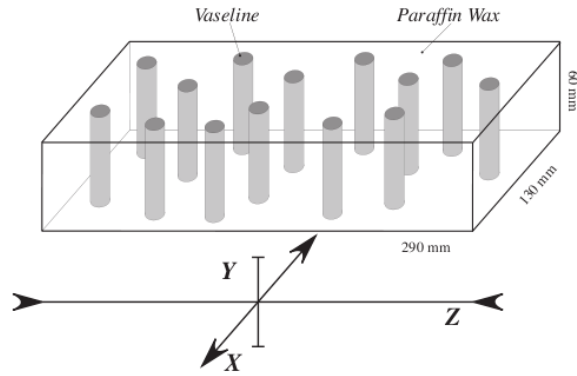


**Figure 4:** Illustration of the main geometrical characteristics of the analogue models in this series of experiments. (Grujic and Mancktelow, 1998). The figure shows a model with 8% Vaseline volume before deformation. The XYZ axes show the orientation of the bulk strain for the imposed deformation. The bulk shortening axis Z, the bulk lengthening axis X, and the bulk intermediate axis Y are labeled in the illustration. The dimensions of the analogue models before any deformation are 290x130x60mm. Cylindrical inclusions of Vaseline are distributed randomly and have cylindrical axes parallel to the intermediate bulk strain axis Y, with circular cross sections in the XZ plane. Vaseline inclusions are the full height of the paraffin wax block, and have a 5mm diameter in the XZ plane.

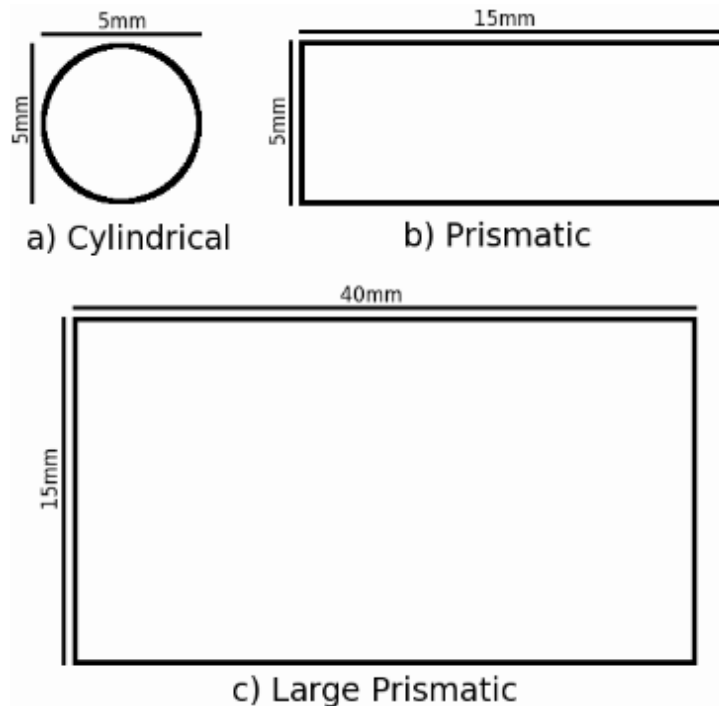


**Figure 5:** Schematic illustration of the Vaseline inclusions in the analogue models when viewed from above (looking along Y axis into the XZ plane, see Figure 4). Illustration is not

to scale. a) Cylindrical inclusions have a circular cross section in the XZ plane, with a 5mm diameter. b) Prismatic inclusions have a rectangular shape in the XZ plane, with edges of length 5mm and 15mm. c) Large Prismatic inclusions have a rectangular shape in the XZ plane, with edges of length 15mm and 40mm. All inclusions are 60mm long along the Y axis, the same length as the analogue model in the Y axis.

Volume percentage of 'melt' in the models is controlled by varying the number of Vaseline inclusions (Table 1). The initial melt-connectivity of the pockets of partial melt in the analogue models is zero due to the impermeability of paraffin wax to Vaseline. Since the Vaseline cannot infiltrate the paraffin wax, the viscosity of the paraffin wax is not a function of the melt fraction within the microstructure. This isolates the effect of the viscosity ratio between the matrix and the weak inclusions on the flow stress and strain localization. Since the melt distribution is unable to reorganize by flowing through the paraffin wax matrix, for shear bands to form, the Vaseline must be deformed over lengthscales greater than the diameter of the inclusions.

| Experiment    | Melt Vol. %  | Inclusions                     | Max Strain | Confining Stress (kPa) |
|---------------|--------------|--------------------------------|------------|------------------------|
| <b>Run 64</b> | <b>0</b>     | <b>None</b>                    | <b>35%</b> | <b>30</b>              |
| <b>Run 84</b> | <b>3.5</b>   | <b>19 Prismatic</b>            | <b>40%</b> | <b>30</b>              |
| Run 87        | 1.5          | 1 Large Prismatic              | 35%        | Unknown                |
| Run 92        | 3.5          | 72 Cylindrical                 | 35%        | 50                     |
| <b>Run 88</b> | <b>6.8</b>   | <b>140 Cylindrical</b>         | <b>40%</b> | <b>50</b>              |
| Run 93        | 10.34        | 213 Cylindrical                | 35%        | 50                     |
| <b>Run 90</b> | <b>13.35</b> | <b>275 Cylindrical</b>         | <b>35%</b> | <b>50</b>              |
| <b>Run 98</b> | <b>21.16</b> | <b>436 Cylindrical</b>         | <b>35%</b> | <b>50</b>              |
| <b>Run 96</b> | <b>28.11</b> | <b>579 Cylindrical</b>         | <b>35%</b> | <b>30</b>              |
| Run 99        | 32.81        | Unknown number,<br>Cylindrical | 37%        | Unknown                |
| Run 94        | 37.72        | 777 Cylindrical                | 35%        | 30                     |

**Table 1:** List of analogue model experiments. 'Melt %' is the volume percentage of Vaseline inclusions in each analogue model. The initial shape of inclusions was either cylindrical or prismatic. Cylindrical inclusions have a circular cross section in the XZ finite strain plane and a cylinder axis parallel to the intermediate strain axis Y. Cylindrical inclusions are 5mm in diameter. Prismatic inclusions are rectangular in the XZ plane with sides of length 5mm and

15mm. Their length in the direction of the intermediate strain axis is the same as the height of the analogue model. Large Prismatic inclusions have sides of length 15 and 40mm in the XZ plane. Rows in bold indicate experiments used for analysis of strain localization and shear band rotation.

### 3.1.4 Analogue Materials

Analogue models consisted of paraffin wax and Vaseline. The paraffin wax used in the modelling had a melting range of 46-48 °C (Mancktelow, 1988b). The viscosity ratio between the paraffin wax and Vaseline is approximately 300:1 at 24±.1 °C at a strain rate of 3x10<sup>-5</sup> s<sup>-1</sup> (Grujic and Mancktelow, 1998).

### 3.1.5 Scaling

As experiments deform the viscous force is partitioned between the matrix and weak inclusions. Assuming 2D deformation of the analogue models with no friction at the top and bottom plates, the force in each materials is given by Equation 4 and Equation 5.

$$F_m = \mu_{MAT} \frac{V}{\Delta L} hw \quad (4)$$

$$F_i = \mu_{INC} Vd \quad (5)$$

where  $F_m$  is the viscous force in the matrix,  $F_i$  is the viscous force in the inclusions,  $\mu$  is the viscosity,  $V$  is the velocity of the compressing pistons,  $h$  is the initial height of the experiment,  $w$  is the initial width of the experiment,  $\Delta L$  is the change in length of the experiment, and  $d$  is the initial lengthscale of the inclusions.

The viscosity of the matrix (Equation 6) is a function of the porosity  $\Phi$  of the matrix (fraction volume of the matrix which is weak inclusions).

$$\mu_{MAT} = \mu_{MAT}(\Phi=0) \exp(-\alpha\Phi) \quad (6)$$

where  $\alpha$  is the melt fraction factor. The melt fraction factor depends on the rheology of paraffin wax, which is unknown under these conditions. However, suspensions of glass, plastic particles, and cold corn syrup return values of approximately ten for the melt fraction factor. We assume that the melt fraction factor of paraffin wax is similar and of order 10. (Jellinek, M., personal communication, 2011)

The ratio of viscous forces in the Vaseline to paraffin wax (Equation 7) governs the response of the analogue model to the applied stress deforming the model. This ratio depends strongly

on  $\Phi$ .

$$\Gamma = \frac{F_m}{F_i} = A \frac{\mu_{MAT}(\Phi=0) \exp(-\alpha\Phi)}{\Delta L} \quad (7)$$

where A is a constant given by Equation 8.

$$A = \frac{hw}{\mu_{INC} d} \quad (8)$$

To measure the evolution of the shear bands, the dimensionless shear band length (Equation 9) is used.

$$A = \frac{L_{sb}}{L_{inc}} \quad (9)$$

where  $L_{sh}$  is the length of a shear band at a particular shortening of an experiment, and  $L_{inc}$  is the lengthscale in the XZ plane of the undeformed inclusions used in the experiment.

### 3.2 Data Analysis

Photographs of the top surface of the analogue model are taken during the experiments by a Hasselblad 503CW middle format camera on 60x60 B&W film. Each experiment is photographed in its initial state, at approximately 2% shortening intervals, and in its final state. Negatives of the film for six experiments were scanned by Dr. Grujic at a resolution of 1400x1400dpi, and saved as digital images with dimensions of approximately 3000x2950 pixels (Figure 6). Table 1 lists the total shortening of each experiment.

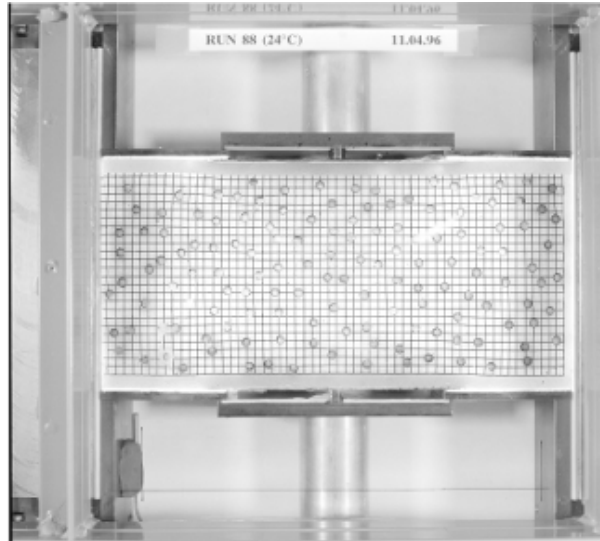


**Figure 6:** Photograph of Run 88 at 32% shortening. Photographs were taken on B&W film and subsequently scanned at a resolution of 1400x1400dpi. The dimensions of images used in this project are approximately 3000x2950 pixels.

### *3.2.1 Image processing*

Digital images of the experiments are processed in three stages that I discuss in turn: (1) images are aligned, (2) strain in the analogue model is calculated, (3) shear bands are identified.

Film negatives of photographs documenting six experiments were scanned by Dr. Grujic to produce digital images. During the scanning process, negatives of the film were centred and aligned in the scanner manually. Slight variations in the image position and image orientation in the scanner resulted in slight variation of the position and alignment of the deformation rig in the images. Each digital image of an experiment during deformation is aligned to the image of the undeformed model using stationary reference points. This removes movement and rotation of the deformation rig and the analogue model between images.

Digital images are aligned using the GIMP image editor using the top and side edges of the label placed on the top plate of the experiment as stationary reference points between images. Each series of digital images of the experiments are aligned using the following routine: 1) A 3200x3200 pixel image is created with a single white layer named BG. 2) The first image of the series, that of the undeformed experiment, is pasted into the image as a new

layer named L1. 3) Layer L1 is shifted so that the analogue model is in the centre of the image. 4) Layer L1 is rotated so that the top edge of the label is horizontal (parallel to the top edge of the image). (Figure 7) 5) A new layer, L2, is created. 6) Three lines are drawn in L2. A line is drawn horizontally across the image to mark the position of the top edge of the label, and two vertical lines are drawn across the image to mark the position of the left and right edges of the label. (Figure 8) 7) Two copies of the image are saved, one as 'background.xcf' which contains and preserves the layers BG and L2, and one as 'Image1.tif' which contains the data from layers BG and L1, with the layer L1 flattened onto the layer BG. 8) 'background.xcf' and the next image in the series are opened. 9) The image of the experiment is pasted as the layer L1 into 'background.xcf'. 10) Layer L1 is shifted and rotated such that the top and side edges of the label align with the lines in L2. (Figure 9) 11) A copy of the image with layer L2 deleted, and Layers L1 and BG merged is saved as 'Image2.tif'. 'background.tif' is not saved. 12) Steps 8 through 12 are repeated for each image in the series.

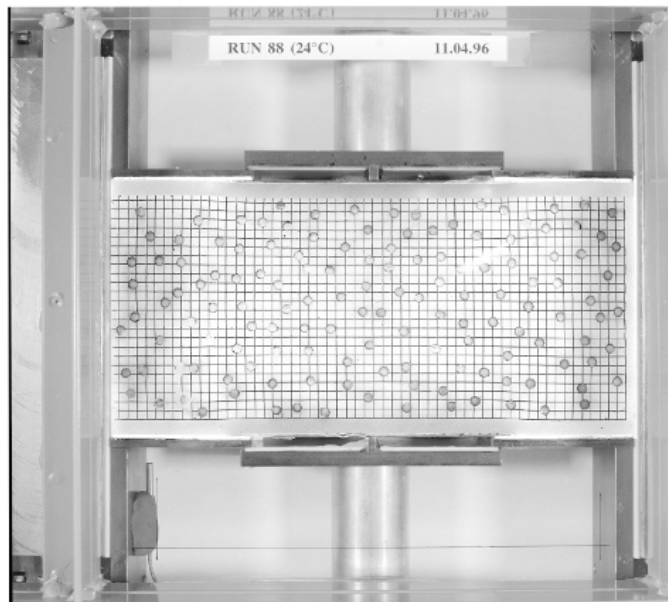


**Figure 7:** Image of the undeformed model in Run 88 placed on a white background. This image is used to align subsequent images in the series.

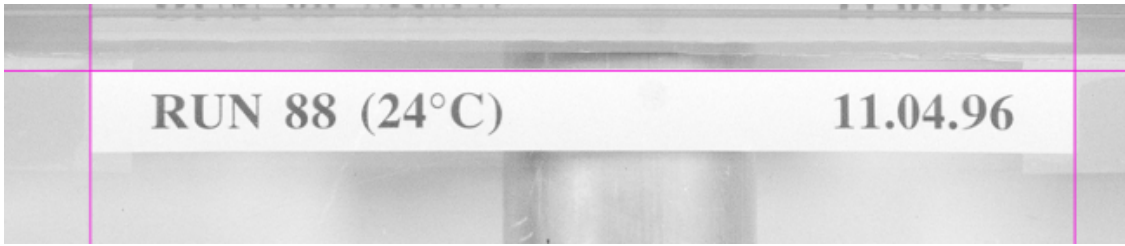


**Figure 8:** Markings indicating the location and orientation of the label on the top plate of the image of the undeformed model. By aligning the edges of the labels on subsequent images to these lines, all images in the series are aligned to image containing the undeformed model. The lines used to align the images are removed before processing the images to determine strain in the model.

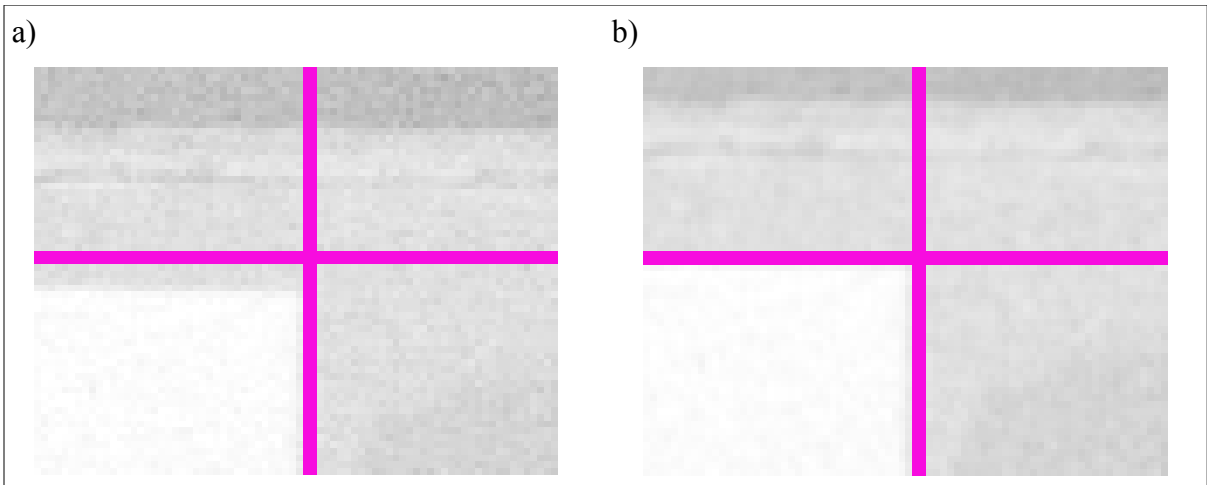
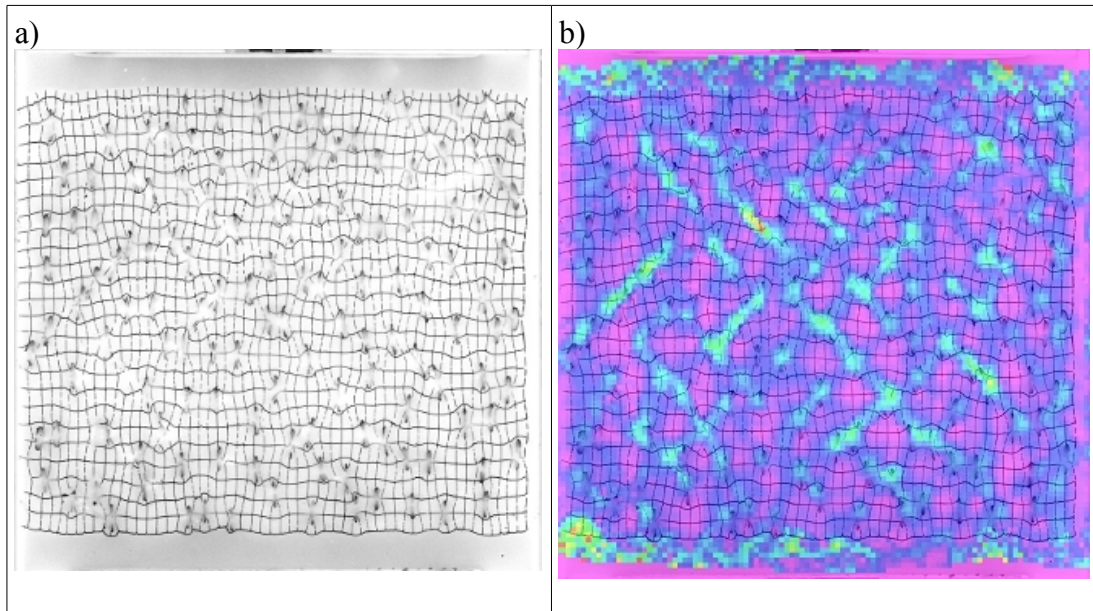


**Figure 9:** Comparison of Run88 at approximately 2% shortening before and after alignment. The image in (a) and (b) is shifted to align the left edge of the label. The image in (b) is rotated to remove a 4 pixel vertical discrepancy between the top right corner of the label and the horizontal line marking the aligned position.

Using this method, images are aligned to an error of  $\pm 1$  pixel in the horizontal and vertical directions, and an error  $\pm 0.05^\circ$  rotation. This results in a potential shift of 2 pixels and a potential rotation of  $0.1^\circ$  between subsequent images.

Strain in the analogue models is calculated using LaVision DaVis Software 7.2 Particle Imaging Velocimetry Software (see Adam, J. et al., 2005). Figure 10 shows successive steps in the processing of the aligned images to calculate the strain on the top

surface of the analogue model. First, the displacement vector field of the top surface of the analogue model is determined between subsequent images in the series (approximately 2% shortening intervals). Each image in a series, except for the first, is compared by the software to the preceding image. The displacement field between the images is determined using multiple passes of an interrogation window decreasing in size. The initial pass uses a window size of 128x128 pixels with 75% overlap, while two subsequent passes are made with a 64x64 pixel window with 50% overlap. Window sizes were chosen empirically. Window sizes smaller than 64x64 pixels contained too little information to accurately determine displacement vector fields. Increasing the number of passes did not yield different results. For very good contrast images, the error in calculated strain values for a 64x64 pixel window  $\sim 0.3\%$ . (StrainMaster Manual). Using the vector displacement fields between subsequent images, LaVision calculates the maximum shear strain in each 64x64 pixel window on the top surface of the analogue model (Figure 10b) accumulated between successive images. The strain accumulated between subsequent images are summed using LaVision to determine the total strain at each image (Figure 10c) (the total strain in each 64x64 pixel window from 0% shortening to the percent shortening of that image).



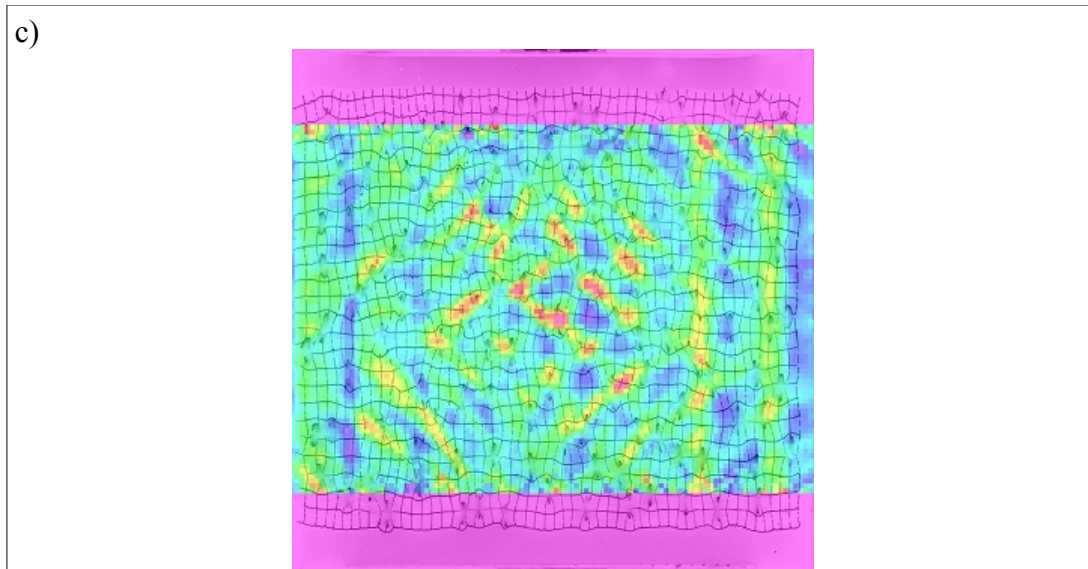
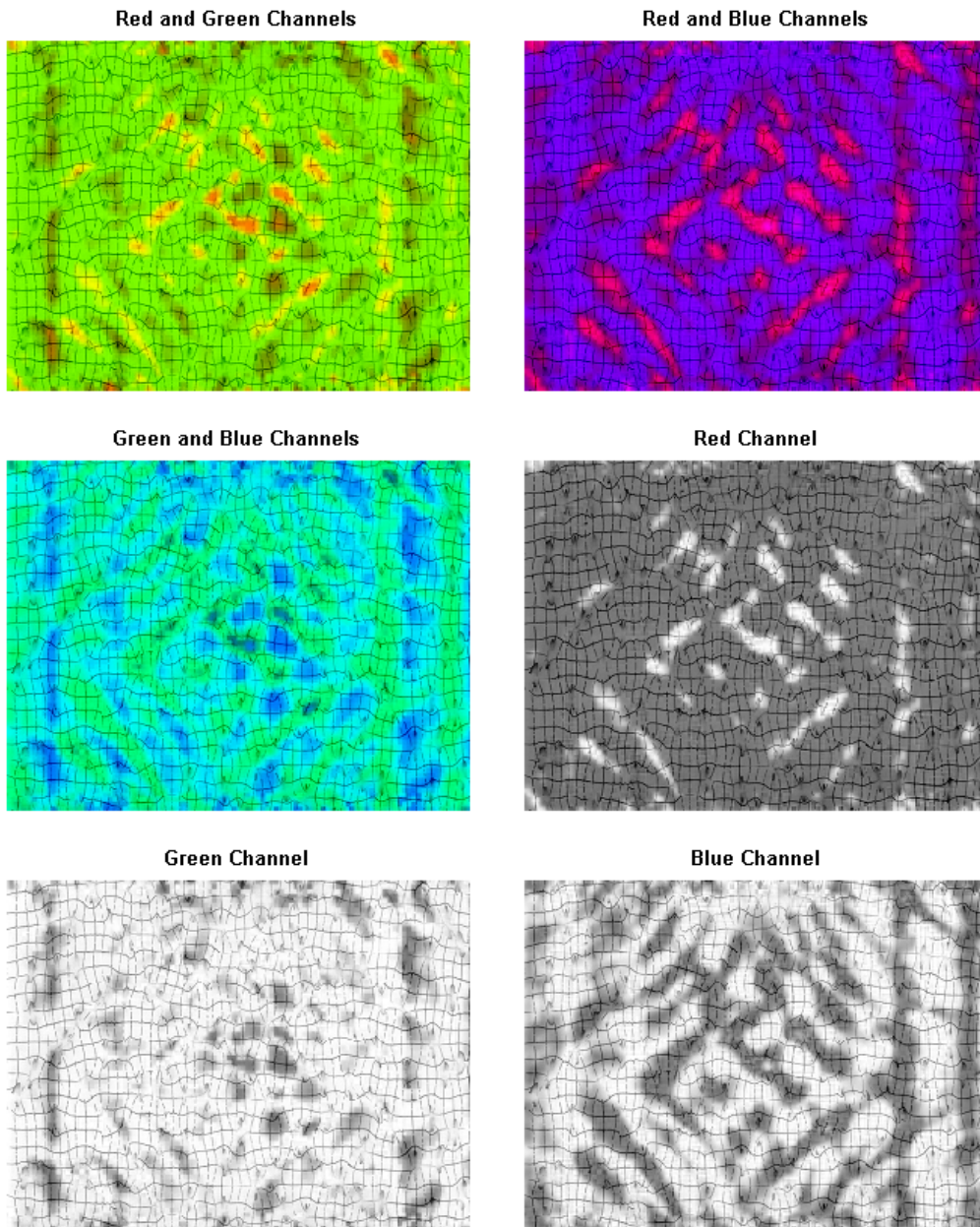


**Figure 10:** Run88 at 32% shortening at progressive steps in the processing procedure. The images have been cropped to show only the top surface of the analogue model. a) Aligned image of the model at 31.7% shortening. b) Davis Image showing incremental shear strain accumulated from 28.7% to 31.7% shortening. c) Surface area of analogue model showing cumulative strain at 31.7% shortening

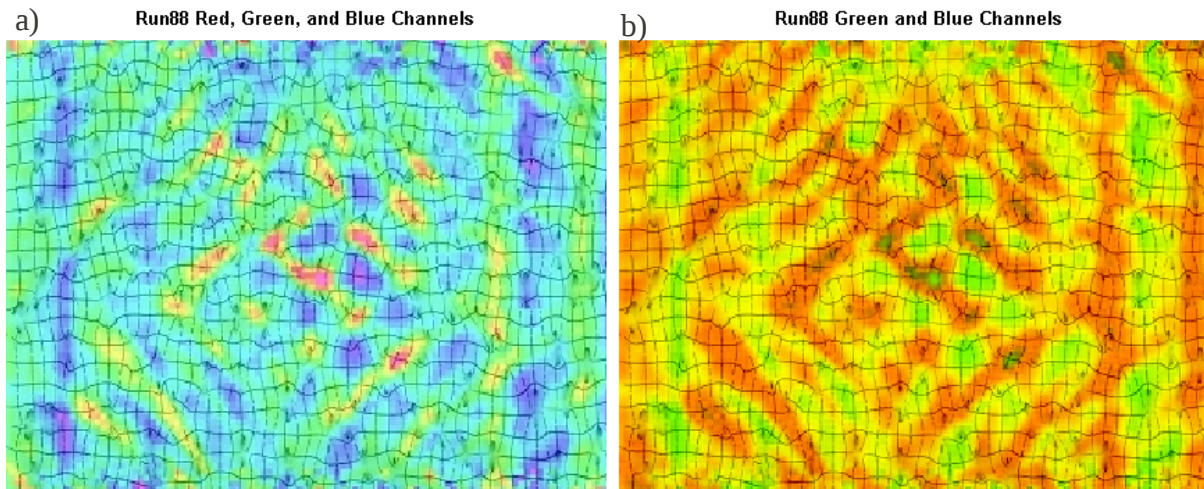
Shear bands are defined as a relatively narrow region in the analogue model over which strain is concentrated. Images of cumulative strain are processed in Matlab to remove color channels not containing information about the edges of shear bands in the analogue models. Removing color channels simplifies the image and allows for better edge detection of shear bands. Images of the cumulative strain on the top surface of the analogue model are saved in a RGB format. Six images are created by displaying pair of color channels (Red-Green, Red-Blue, Green-Blue) and each color channel individually. (Figure 11). Each image is inspected visually to determine if there is a saturated color channel. Saturated color channels do not contain information useful in determining shear bands in the analogue model since the color does not contain information on levels of strain which are seen in the model at the stage of deformation. Images of the strain distribution are recomposed using channels identified as non-saturated. For visual consistency, images recomposed of two channels use a red-green color scheme, with red indicating areas of high strain and green indicating areas of low strain.

Figure 11 illustrates the effect of subtracting the red channel of an image of Run 88 at

32% shortening. A combination of the green and blue channels was selected qualitatively as the image best showing the shear bands, since the red channel is uniform over a large portion of the image. In the RGB image of Run 88 at 32 shortening, areas of red and dark purple indicate areas of the greatest strain (Figure 12a). These areas appear as dark green in the image with green-blue channels (Figure 12b).



**Figure 11:** Strain calculations in Run88 at 32% shortening displayed using pairs and individual color channels.



**Figure 12:** Cumulative strain in Run88 at 32% shortening displayed using all color channels, and the green-blue color channels.

To quantify the deformation in the analogue models, shear band lengths at different stages of deformation are measured. Shear bands are determined qualitatively in each of the images after saturated color channels are removed. Since shear bands are areas of concentrated strain, the color representing the average strain undergone in the experiment is selected as the edge of shear bands. This color varies between experiments since experiments have different ranges between maximum and minimum strain amount, and different color channels contain information about different parts of this range. The color best representing the average strain was determined by investigating the color transition between areas undergoing low amounts of strain adjacent to areas undergoing high amount of strain (Figure 13). A representative transition zone was selected, and the color that in the middle of the transition was selected as the boundary between areas of high strain and low strain. This color was used to determine the edges of shear bands.

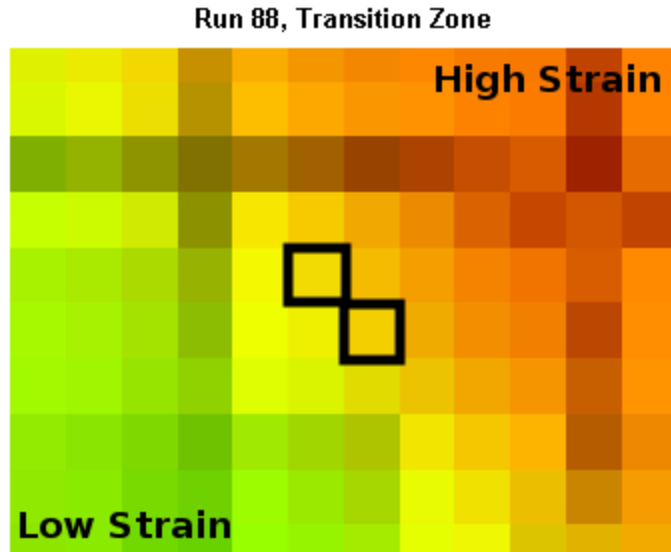


**Figure 13:** Transition zone between high strain and low strain. The color in the centre of the transition was selected as best representing average strain in the model.

Shear bands are identified in the images as relatively long narrow regions of greater than average strain. A pixel that is redder than the color selected to represent the boundary of shear zones is said to have greater than average strain. For an area of concentrated strain to be identified as a shear zone, the width of the area has to be greater than the diameter of inclusions, and the length has to be greater than twice the width. An area that forms a shear band must be at an angle greater than  $10^\circ$  to the horizontal, but not greater than  $80^\circ$ . The interval on the angles of shear bands is imposed to prevent the classification of the vertical areas of high strain as shear bands.

Shear bands are measured in pixels using the ruler tool in Matlab (Figure 14). Shear bands are measured from the center of one end of the band to the center of the opposite end of the band. Each shear band is measured three times, and the length of the shear band is the average of the three measurements. If a shear band intersects the edge of the analogue model, the edge of the model is used as the point the shear band ends.

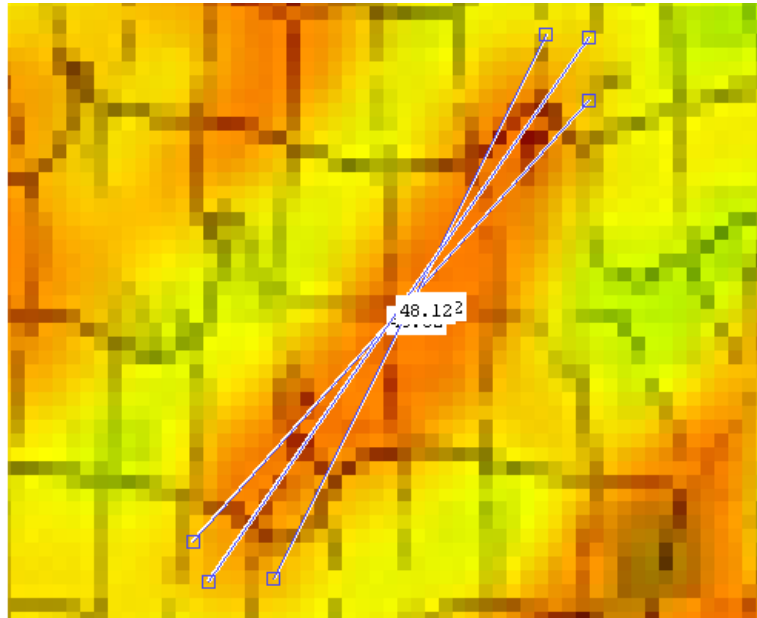


**Figure 14:** Measuring shear bands using the ruler tool in Matlab.

## 4. Results

### 4.1 Flow Stress

The flow stress of an experiment (Table 2) is defined as the average value of the applied differential stress in the segment of the smoothed stress-strain curve over which the stress is independent of the strain. Stress-strain curves (Figure 15) for analogue models with increasing volume percentages of partial melt have similar shapes and are composed of four regimes. Regime 1 is the segment of the stress-strain curve where stress increases linearly with strain. This regime occurs from 0% to approximately 1.75% shortening. Regime 2 is the rounded part of the stress-strain curve and occurs from approximately 1.75% to 6.5% shortening. Regime 3 is the segment of the stress-strain curve where the stress is independent of the strain. This regime occurs between approximately 6.5% to 11.3% shortening. Regime 4 is the segment of the stress-strain curve where stress decreases as a function of strain. It occurs from approximately 11.3% shortening until the end of the experiment.

| Vol. % Melt | Flow Stress Average (kPa) | Deviation ( $\pm$ kPa) |
|-------------|---------------------------|------------------------|
| 0           | 70.94                     | 2.12                   |
| 1.5         | 68.87                     | 2.02                   |
| 3.5         | 62.08                     | 1.54                   |
| 6.8         | 58.52                     | 1.57                   |
| 10.34       | 51.24                     | 1.98                   |
| 13.35       | 49.69                     | 1                      |
| 21.16       | 39.58                     | 1.94                   |
| 28.11       | 32.31                     | 1.98                   |
| 32.81       | 32.39                     | 2.37                   |
| 37.72       | 25.49                     | 1.11                   |

**Table 2:** Volume percent melt of analogue models and their corresponding flow stress. Volume percentage melt is determined when creating the analogue models. The flow stress was calculated by taking the average value of stress-strain in the segment where stress is independent of strain.

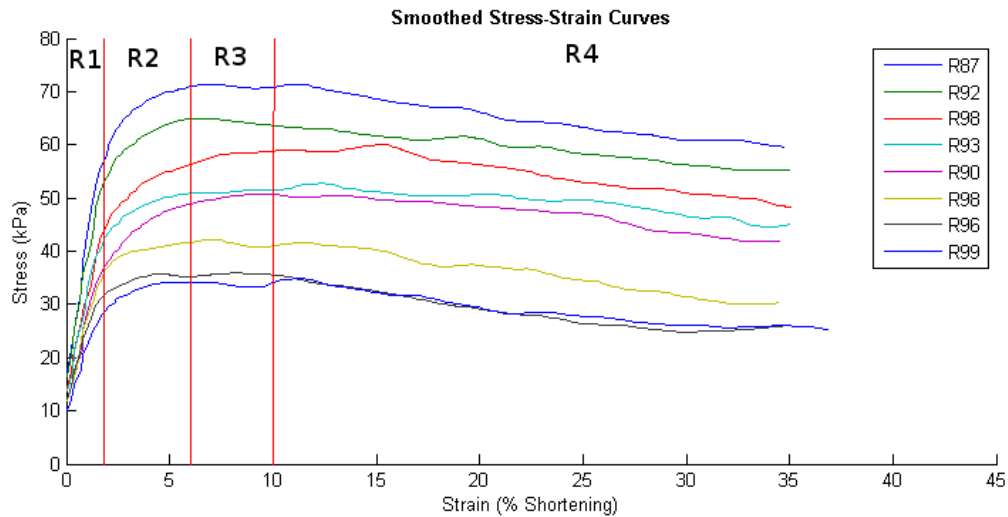


**Figure 15:** Stress-strain curves plotted for eight analogue model experiments. Each stress-strain curve can be decomposed of four regimes. Regime 1 is the segment of the stress-strain curve where stress increases linearly with strain. Regime 2 is the rounded part of the stress-strain curve. Regime 3 is the segment of the stress-strain curve where the stress is independent of the strain. Regime 4 is the segment of the stress-strain curve where stress

decreases as a function of strain.

Volume percentage melt against flow stress is plotted in Figure 15 and fitted empirically with Equation 10.

$$y = 69.57811 \cdot 0.97444^x \quad (10)$$

The  $R^2$  value of the fit is 0.99.

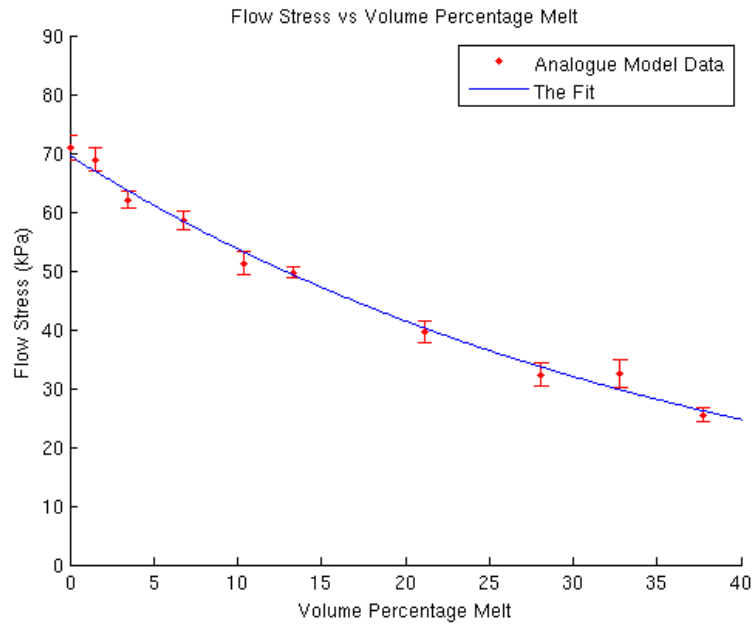


**Figure 16:** Plot of flow stress against volume percentage melt for ten analogue model experiments. The mean flow stress is determined from the stress-strain curves. The data points are fit with  $y = (69.57811) \cdot (0.97444.^x)$ . The  $R^2$  value of the fit, indicative of the quality of the fit, is 0.99.

#### 4.2 Strain Localization in Images

To understand the relationship between the flow stress and strain, images of the analogue models are analyzed using particle imaging velocimetry to characterize the distribution of strain. The strain distribution in Run 64, containing no Vaseline inclusions, is determined and compared to models containing partial melt to determine the influence of low viscosity inclusions on strain distribution. Images of five experiments are analyzed at low levels of shortening to determine the level of shortening at which shear band networks form. The length of shear bands in five experiments are measured at three stages of deformation to

investigate the relationship between dimensionless shear band length and force partitioning between the Vaseline and paraffin wax.

#### 4.2.1 Boundary effects and strain localization on low viscosity inclusions

Experiments with low viscosity inclusions develop a different strain distribution than the experiment with no inclusions. Run 64, Run 88, and Run 98 are compared at 26% shortening to determine the influence of low viscosity inclusions (Figure 17). The heterogeneous strain distribution in Run 64 at 26% shortening is investigated to determine the boundary effects of the deformation rig on the analogue models. The distribution of the Vaseline inclusions at 33% shortening (Figure 18) is compared to the strain distribution to investigate strain localization.

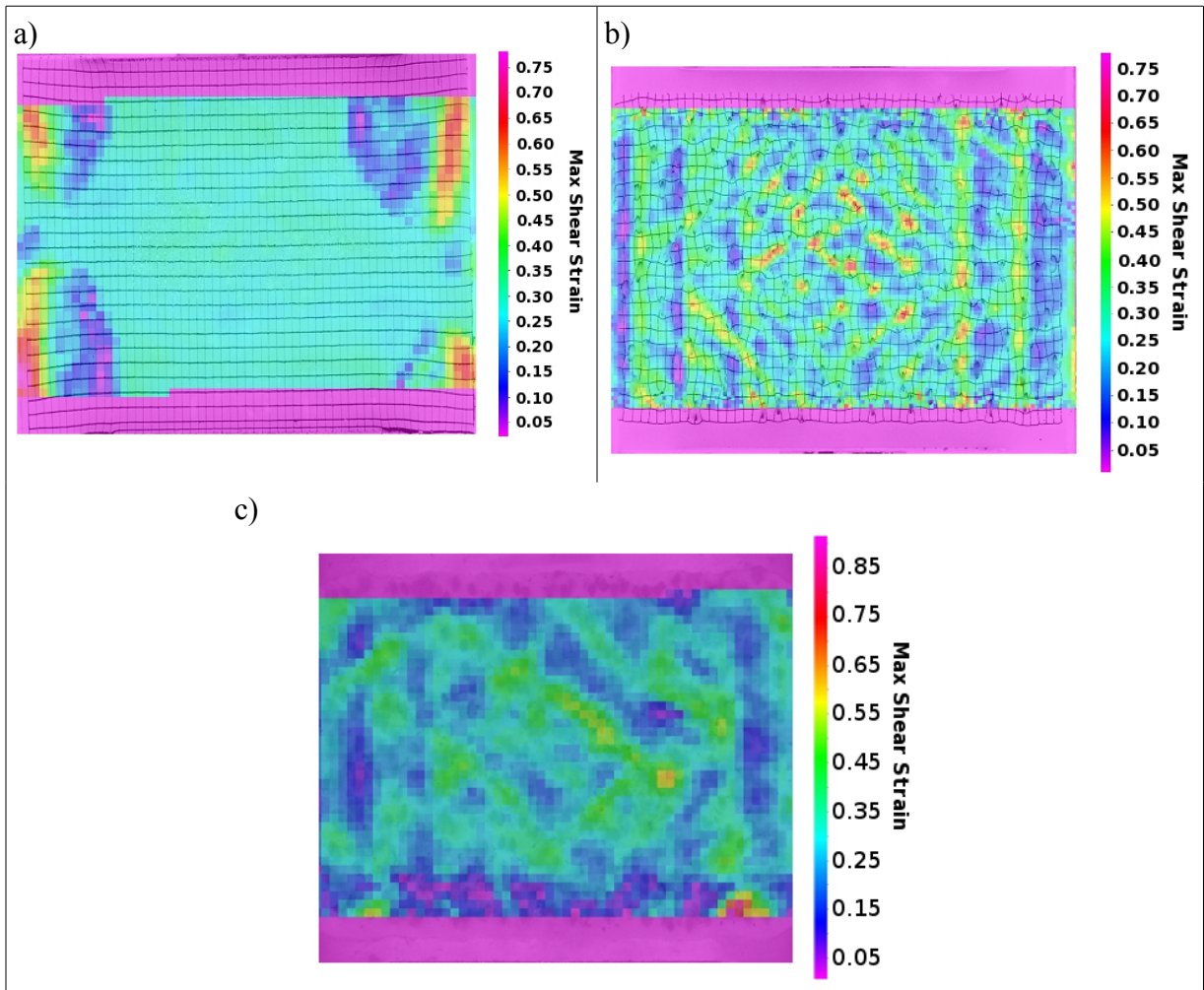


**Figure 17:** Comparison of a) Run 64 , b) Run 88, and c) Run 98 at 26% shortening. Boundary affects of the deformation rig can be seen in (a). While there are clear boundary affects in the corners of the analogue model, the centre of the model is deformed homogeneously. Images (b) an (c) show strain localization due to weak inclusions.

At 26% shortening Run 64 has homogeneous distribution of strain in the centre of the model, with heterogeneous pockets of strain in each corner. Strain values in the centre are between 0.25-0.30. The distribution of strain in each corner of Run 64 follows a similar pattern. On the outside edge of each corner there is a band of higher strain following the  $X$  bulk strain direction. Strain values in these bands range between 0.50 and 0.65. On the inside edge of the higher strain band there is a region of strain values between 0.03 and 0.18. There is a narrow transition zone between the region of high and low strain. The maximum and minimum strain in Run 64 at 26% shortening are 0.78 and 0.021. Regions of lower strain have strain values 07-0.27 less than the centre, while regions with higher strain have strain values 0.20-0.40 greater than the central region. Regions of high strain experience a greater deviation from the centre than regions of low strain. The size of the area over which strain is distributed heterogeneously varies between the corners. The area is largest in the top right and bottom left corners, and smallest in the bottom right corner. In an ideal experiment, the distribution of strain in the experiment would be homogeneous. The heterogeneities in the corners of the model are boundary effects of the deformation rig. These effects are neither isotropic nor symmetric.

Run 88 at 26% shortening has concentrated areas of higher strain forming shear bands and areas of matrix undergoing lower amount of strain. Areas of high and low strain occur over the whole model. On the left and right side of the model are two vertical bands of high strain. Strain concentrates in bands in the centre of the model oriented at an angle to the horizontal. Areas of concentrated strain have widths on the lengthscale of inclusion diameter, and are much longer in length. In all regions of the model are small areas of strain greater than 0.55 located on Vaseline inclusions. The maximum and minimum strain in the model are approximately 0.75 and 0.05 respectively.

Run 96 at 26% shortening has concentrated areas of higher strain and lower strain throughout the model. Strain ranges from approximately 0.05 to 0.7. The majority of the

model undergoes a strain within the range of 0.1-0.5. There are three relatively small areas of the model undergoing strain greater than 0.6. Near the bottom edge of the model are several small areas undergoing strain less than 0.05. Areas of concentrated strain in the model are longer and wider than the lengthscale of the inclusions.

Run 98 at 33% shortening has weak inclusions located in areas experiencing low amounts of strain (Figure 18). Not all weak inclusions are associated with a shear band.

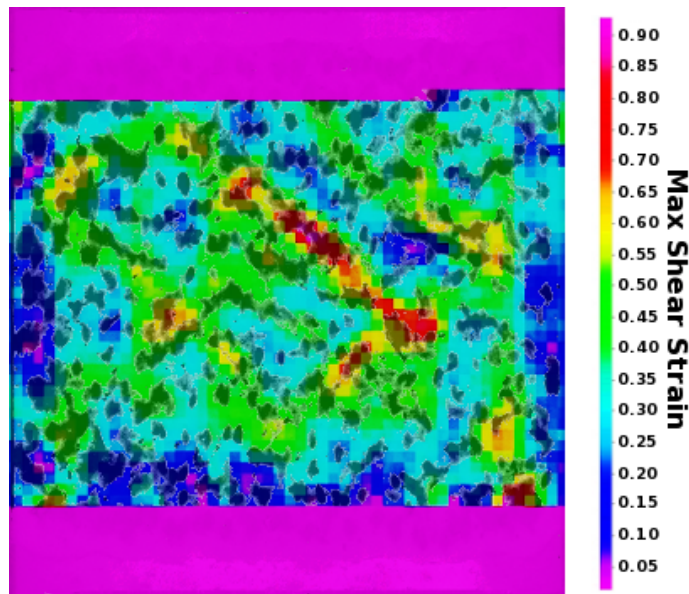


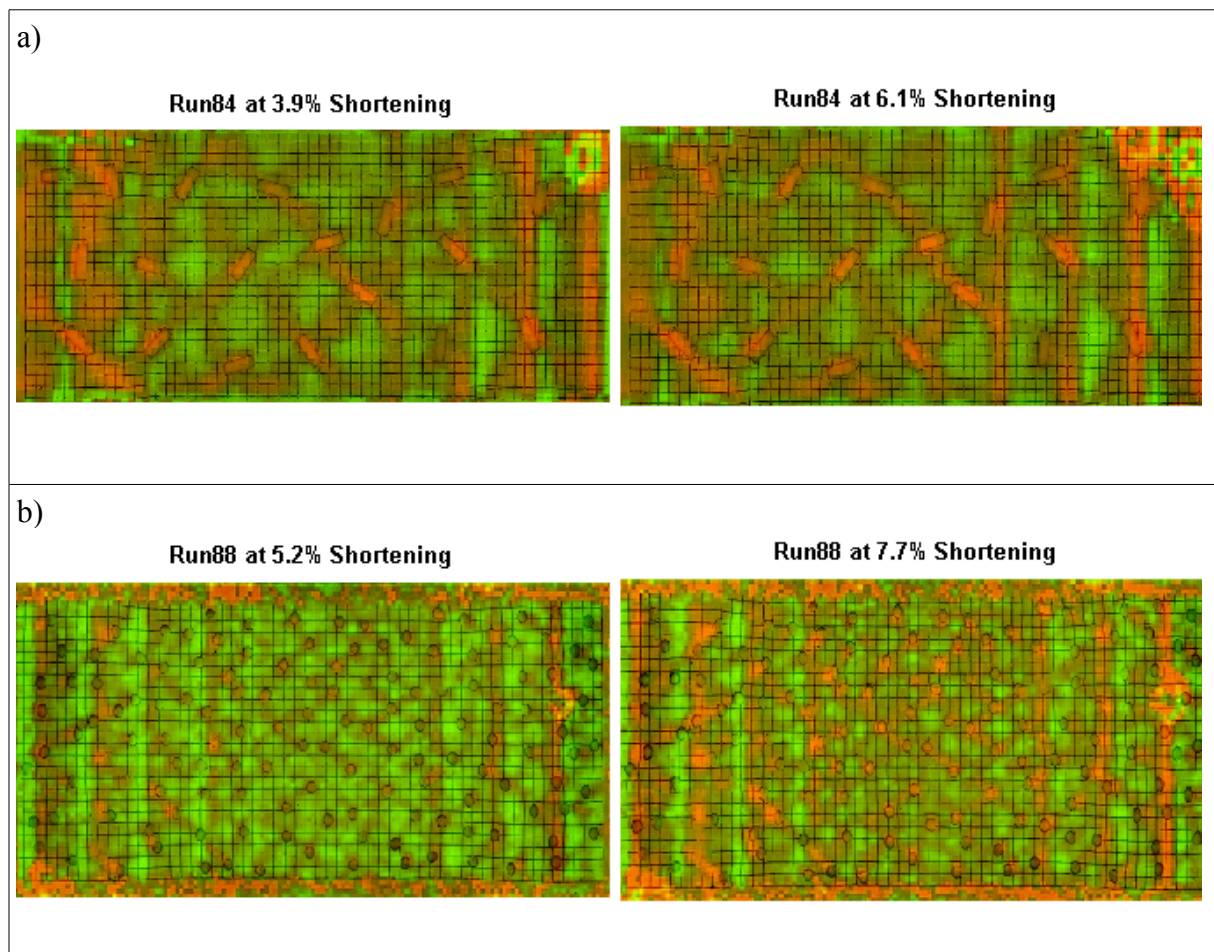
**Figure 18:** Image of Run 98 at 32% shortening showing strain distribution. Overlain on the processed image in dark gray are the deformed vaseline inclusions from the unprocessed image. Not all weak inclusions are associated with a shear band, with weak inclusions located in areas undergoing low amounts of strain.

#### 4.2.2 Shear bands

As analogue models deform, areas of high strain develop around weak inclusions. With progressive shortening, areas of high strain connect forming shear bands. Images of five experiments are investigated at three stages of deformation. 1) when shear band networks form 2) at 19.5% shortening 3) at 32% shortening. A shear band network is defined as an interconnected system of throughgoing shear bands connecting low viscosity inclusions separated by areas undergoing lower amounts of strain. Images when shear band networks

form rather than when shear bands appear were chosen as the earliest stage of deformation to investigate because of the difficulty of determining when shear bands appear at low stages of deformation. Because images are taken at 2% shortening intervals, and are limited by their resolution, it is easier to consistently identify when shear band networks form in experiments than when shear bands appear. Images at later stages of deformation are analyzed to determine the evolution of shear bands in the analogue models as the experiments are deformed.

The percent shortening of the models at which shear band networks is determined visually (Figure 19, Table 3).



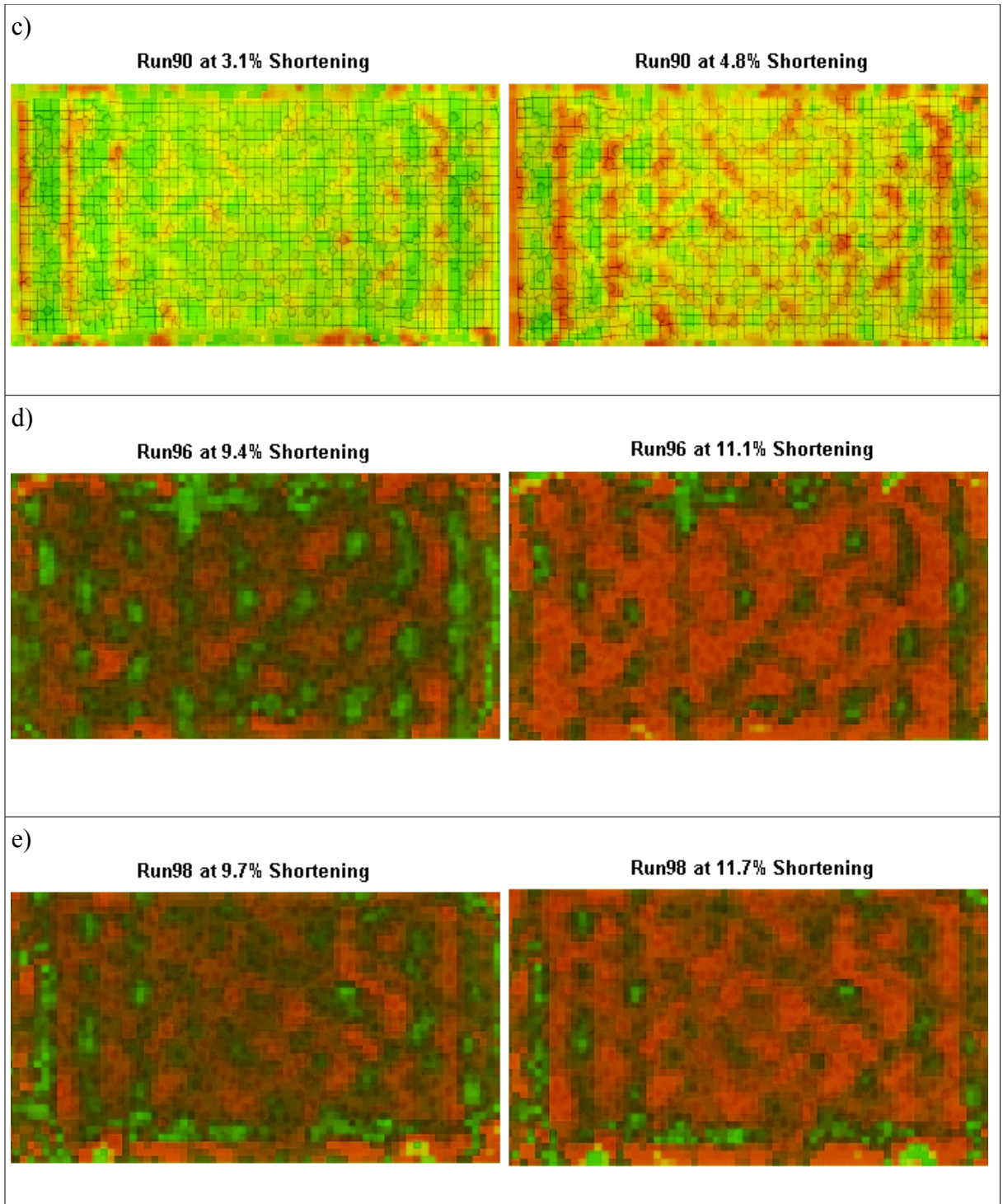


**Figure 19:** Images of the strain distribution of the analogue models showing the deformation interval at which shear band networks form. The values of the deformation steps are in Table 5. Images: (a) Run 84 (b) Run 88 (c) Run 90 (d) Run 96 (e) Run 98.

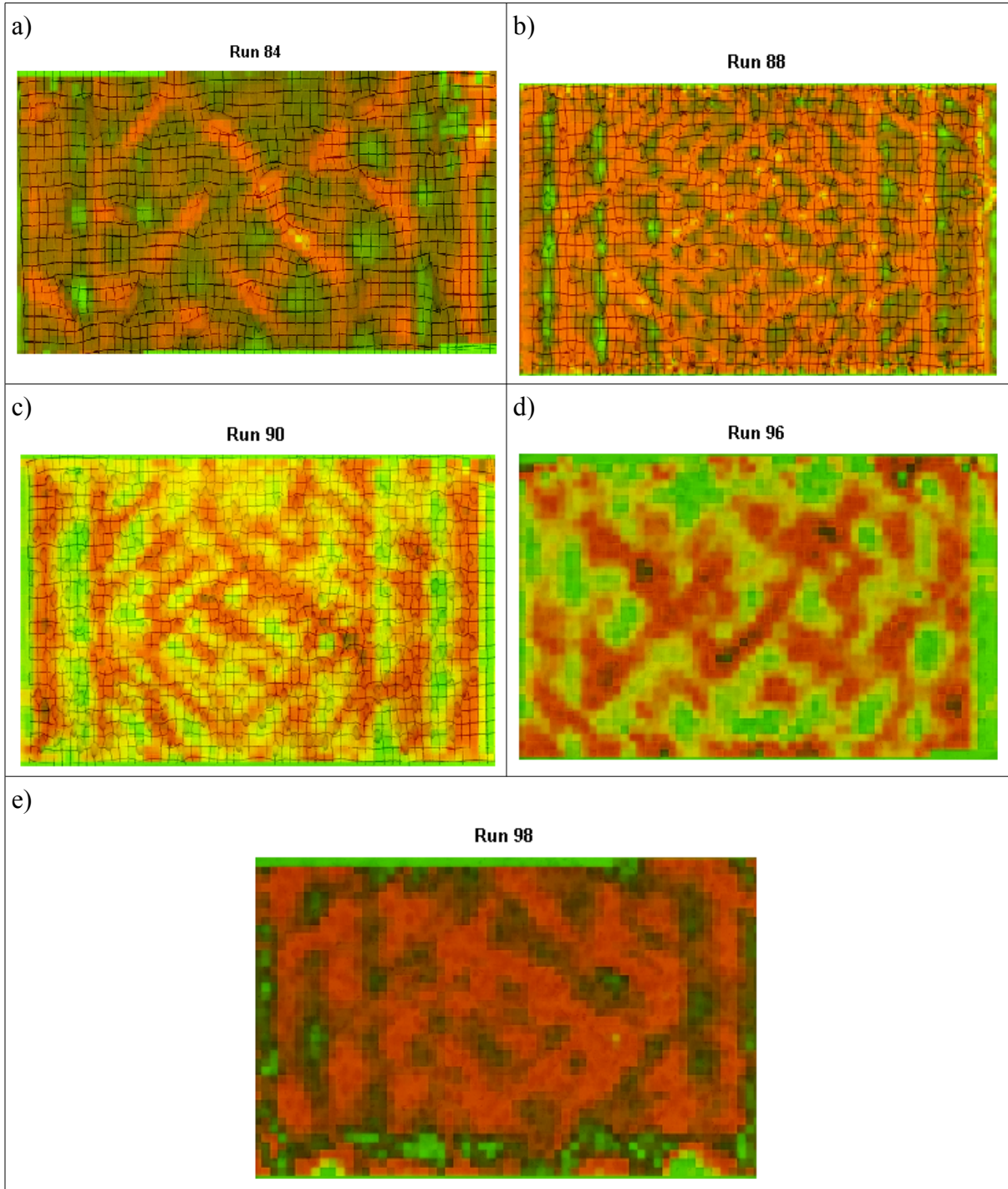
| Experiment | Vol. % Melt | Shortening (%) |
|------------|-------------|----------------|
| Run 84     | 3.5         | 3.9-6.1        |
| Run 88     | 6.8         | 5.2-7.8        |
| Run 90     | 13.35       | 3.1-4.8        |
| Run 96     | 28.11       | 9.4-11.1       |
| Run 98     | 21.16       | 9.7-11.7       |

**Table 3:** Percentage shortening of each experiment at which a shear band network appeared.

Run 84 develops a shear band network between 3.9% and 6.1% shortening. Shear bands are visible in the processed image at 3.9% shortening, but do not connect low viscosity inclusions. Shear bands form both parallel and perpendicular to the longest direction of the prismatic inclusions. Run 88 forms a shear band network between 5.2% to 7.8% shortening. At 5.2% shortening, there are multiple regions of high strain that approach or slightly exceed meeting the criteria of being classified as a shear zones. However, accurately determining whether their length is greater than twice the width is not possible. Between 3.1% shortening and 4.8% shortening, Run 90 sees a substantial localization of strain. At the resolution of our images, strain begins to be localized on the Vaseline inclusions at 3.1%, with several nascent shear bands beginning to form on the centimeter scale. At 4.8% shortening, shear bands on the scale of  $10^1$  cm are visible. Run 96 has regions of strain localization at 9.4% shortening on the centimeter scale which do not have a defined direction since their length is not substantially greater than their width. At 11.% shortening, shear bands are on the scale of  $10^1$ cm. Shear bands in Run 98 form in the range of 9.7% to 11.7%.

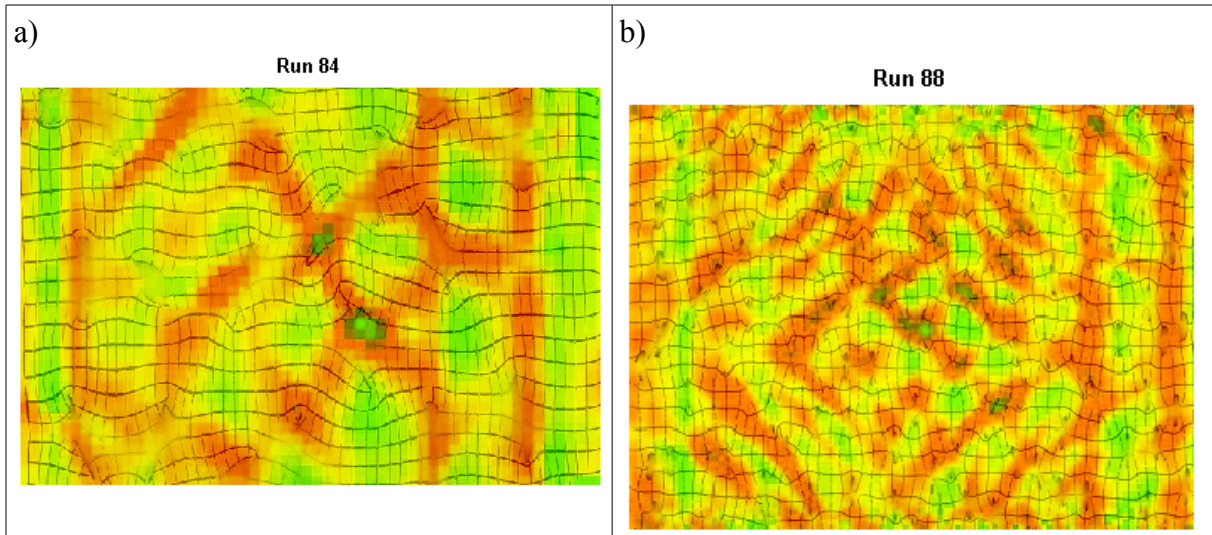
At 19.5% shortening shear bands become more visible due to larger difference in strain between areas of high strain and low strain (Figure 20). Shear bands in Run 84 have the same pattern as at 6.1% shortening but are wider. Shear bands in Run 88 are longer and wider. Run 90 has a dense pattern of shear bands in the centre of the experiment, with no shear bands near the left and right edges. Shear bands have increased in length and width. The number of shear bands in Run 96 is lower than in Run 88 and Run 90, but the shear

bands are substantially wider and longer. The length and width of shear bands in Run 98 has increased from the earlier stage of deformation.



**Figure 20:** Images of the strain distribution in each analogue model at 19.5% shortening.

At 32% shortening, each experiment developed a well defined network of shear bands (Figure 21). Run 84 has a network with the same number of shear bands as in previous levels of deformation, with similar lengths and widths. In Run 88 regions of low strain on the lengthscale of inclusion diameter have disappeared or coalesced to form larger regions. In Run 90 the number of shear bands has been reduced, and their width increased. Run 96 and Run 98 have wider shear bands since areas of high strain that were not shear bands at earlier stages are incorporated into existing shear bands.



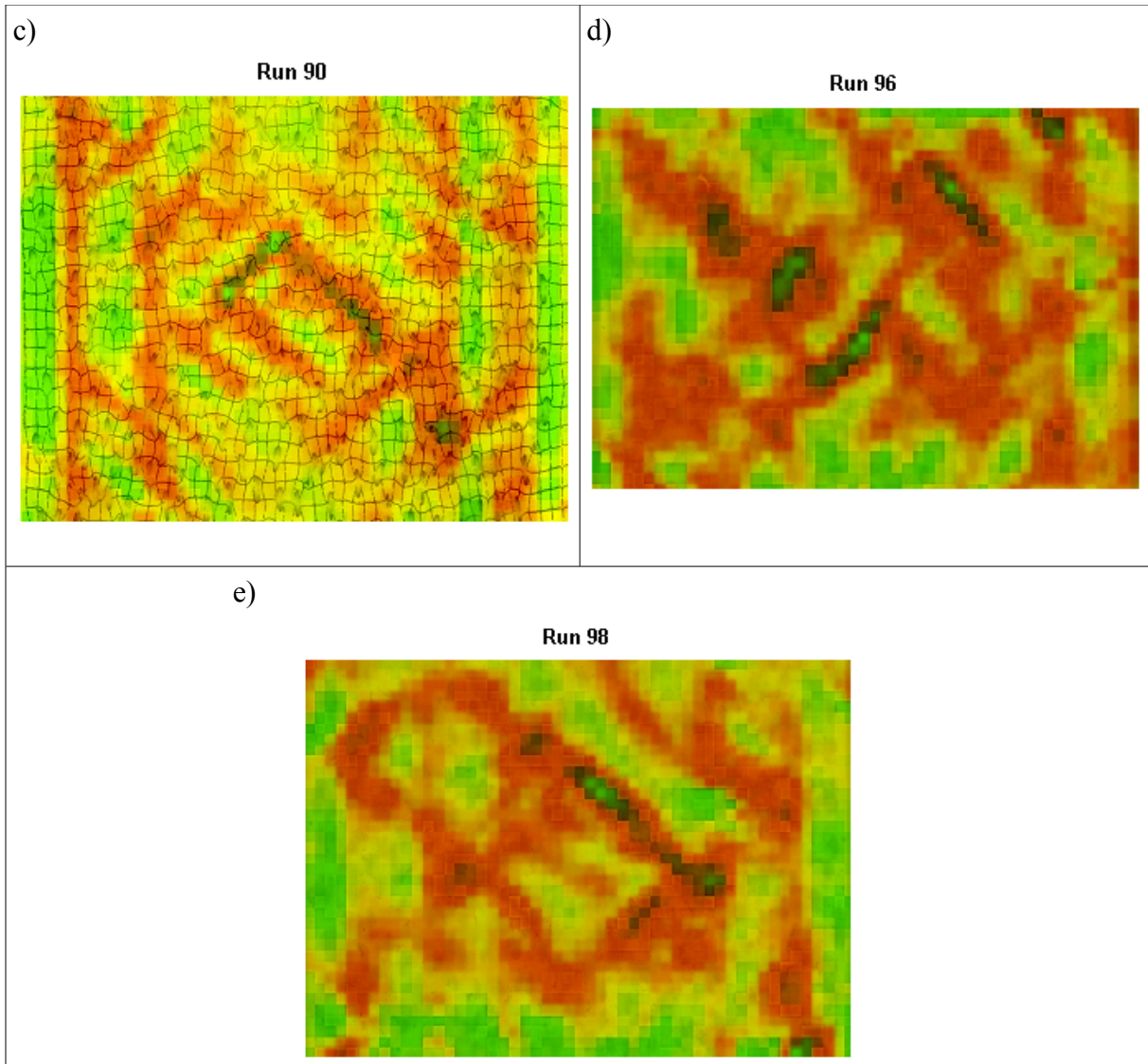
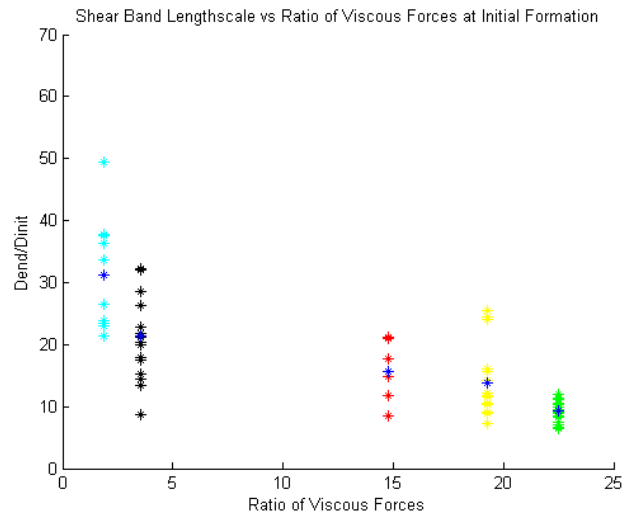


**Figure 21:** Images of the strain distribution in each analogue model at 32% shortening.

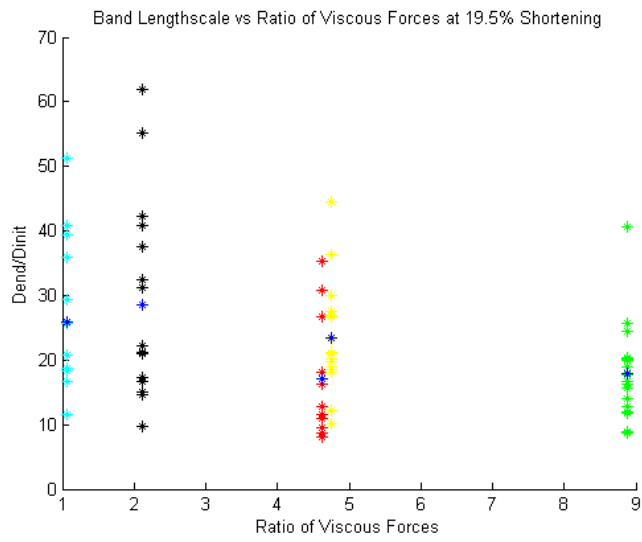
#### 4.3 Deformation

Deformation within the analogue models is determined at three stages of shortening using the dimensionless shear band length  $\Lambda$  (Equation 9) of observed shear bands. Measurements of the deformation are made at the upper end of the interval of shortening when shear band networks appear (Table 3), 19.5% shortening, and 32% shortening. I investigate whether the deformation of the analogue models is a function of  $\Gamma$ , the ratio of stress in the paraffin wax to stress in the Vaseline (Equation 7).

a)



b)



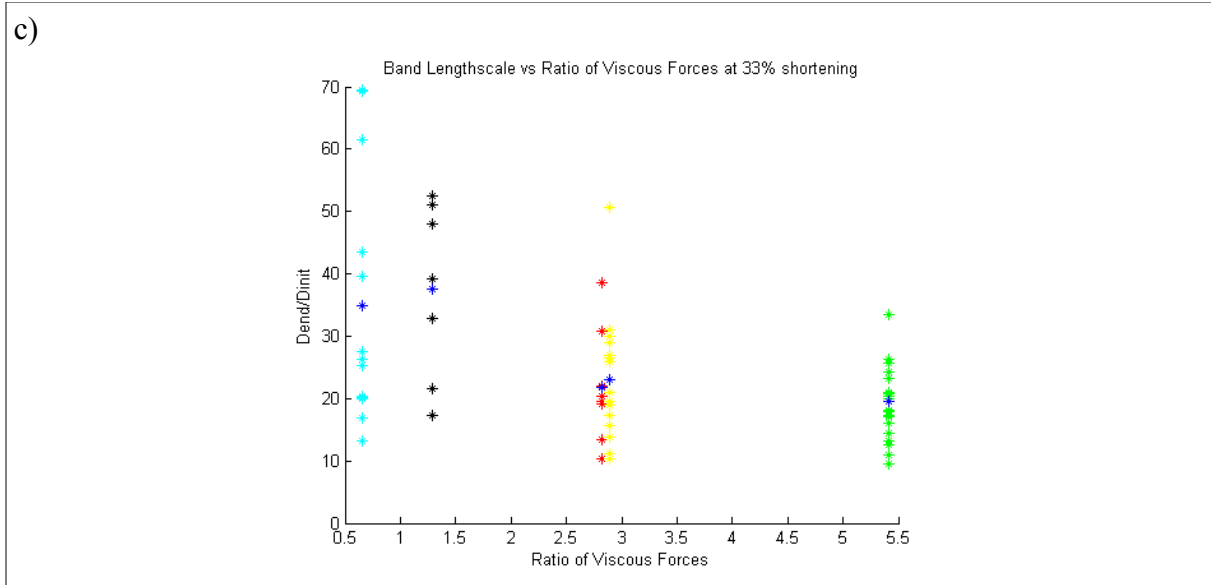


**Figure 22:** Dimensionless lengthscale of shear bands vs ratio of viscous forces in analogue models at three shortening levels. Shear band lengths of Run84 are red, Run88 are green, Run90 are yellow, Run96 are cyan, Run98 are black. The mean shear band lengthscale of each experiment is a blue point.

At the levels of shortening at which shear band networks were determined to appear the maximum and minimum mean value of  $\Lambda$  for the set of experiments is 31 and 9 respectively. The maximum mean value occurs at  $\Gamma=2$  and the minimum mean value is at  $\Gamma=22.5$ . Over the interval of  $\Gamma$  in Figure 22a,  $\Lambda$  decreases with increasing  $\Gamma$ .

At 19.5% shortening, the minimum value  $\Gamma$  decreased by .9 to 1.1 and the maximum value of  $\Gamma$  decreased by 13.6 to 8.9. At  $\Gamma=1.1$  and  $\Gamma=2.1$ , the mean value of  $\Lambda$  is 26 and 29 respectively. At approximately  $\Gamma = 4.7$ , the mean value of  $\Lambda$  is between 17 and 23. At  $\Gamma=8.9$ , the mean value of  $\Lambda$  is 18.  $\Lambda$  decreases by approximately 10 over the interval of  $\Gamma$  at this stage of deformation. Though a decrease in  $\Lambda$  as function of  $\Gamma$  is observed over this interval of strain partitioning, the degree of dependence of  $\Lambda$  on  $\Gamma$  is unclear due to the large variability in values of  $\Lambda$  for each experiment. The value of  $\Lambda=29$  at  $\Gamma=2.1$  is comparable with the value of  $\Lambda=31$  at  $\Gamma=2$  in Figure 22a..

At 32% shortening,  $\Gamma$  is between 0.6 and 5.4. The mean values of  $\Lambda$  at  $\Gamma=0.6$  and at  $\Gamma=1.3$  are 35 and 38 respectively. At  $\Gamma$  equal to approximately 2.7, the mean value of  $\Lambda$  for two experiments is approximately 21. These values are similar to the value of  $\Lambda=3.5$  in

Figure 22a at  $\Gamma=3.5$ . The value of  $\Gamma$  decreases to 19 at  $\Gamma=5.4$ . Similar to the models at 19.5% shortening, we see a decrease in  $\Lambda$  as a function of  $\Gamma$ .  $\Lambda$  decreases by approximately 18 over this interval.

## 5. Discussion

### 5.1 Implications for Rheology

As partial melt increased, the flow stress of our experiments decreased. (Figure 16). A non-linear relationship between flow stress and volume percent melt produced the best fit curve (Equation 10). The relationship between flow stress and increasing volume partial melt is strongest at low levels of partial melt. It is hypothesized that this is a result of the ratio of stresses  $\Gamma$  in the models being influenced by additional low viscosity material strongest at low volumes of melt (Equation 7). For a given applied flow stress, the low viscosity material will flow much faster than the high viscosity material. At small volumes of melt, a small increment increase in melt will increase the proportion of stress in the low viscosity material greater than at high volumes melt. A small increment increase in melt will also increase the relative proportion of melt greater at low volumes percent of partial melt than at high volumes percent partial melt.

Although our data set is fit with a non-linear curve, the deviation from a linear fit is small. The relationship between flow stress and volume percent partial melt in our data is similar to the linear relationship observed by Takeda and Obata (2003) in rock mechanics experiments, and contrasts with the experimental data compiled by Rosenberg and Handy (2005) showing a strong non-linear relationship. The role of permeability in the different experiments is thought to be important in explaining the different relationship observed and is discussed in Section 5.2.

Over a melt volume from 0% to 37.72% the flow stress of analogue models decreased an order of magnitude of  $10^1$ . Rock deformation experiments investigated by Rosenberg and Handy (2005) reduced in viscosity from an order of  $10^3$  to  $10^{-3}$  over a similar melt fraction. The larger drop in viscosity seen in rock mechanic experiments is likely due to stronger strain softening from processes such as crystallization, melting feedback, and

evolution of grain shape and size not simulated by our analogue materials.

## 5.2 Critical Melt Fractions and the Role of Impermeability

We do not observe a significant drop in flow stress of the models in the interval of 10-30% melt corresponding the RCMP. This contrasts with data from rock mechanics experiments (Figure 1) compiled by Rosenberg and Handy (2005). The configuration of Vaseline in the analogue models is similar to the configuration of crystallizing magma proposed by Vigneresse (1996). For a framework-supported rheology, Vigneresse (1996) predicted the RCMP lies within 25-45% volume melt. There is no significant decrease in flow stress between 25% and 37.72% volume melt in our analogue models.

Rosenberg and Handy (2005) observed an ~90% viscosity drop in deformation experiments between melt volume of 0% and 7%. Though our analogue models do not simulate the process of grain boundary wetting, the proposed explanation behind the significant viscosity drop, we do observe flow stress to be most dependent on melt fractions at low percentages volume melt.

A crucial difference between the analogue models analyzed and rock mechanics experiment is the permeability of the high viscosity matrix. A permeable matrix permits the redistribution of low viscosity material by pressure gradients within the experiment. Since paraffin wax is impermeable to Vaseline, at low strains our experiment has a permeability of zero. Over large strains the distribution of Vaseline inclusions is not static and the permeability is non-zero.

The model of strain localization proposed by Stevenson (1989) predicts that low viscosity fluid flows towards areas where fluid has already accumulated. Localized areas of high viscosity matrix containing greater percent volumes of partial melt than neighboring regions will have a lower mean stress due to a decrease in viscosity. Gradients in mean stress result in a feedback forming melt-rich shear bands enclosing areas of melt-depleted matrix. Since our high viscosity matrix is impermeable, we do not see the Vaseline reorganizing into melt rich and melt-depleted areas by flowing through the micro structure of paraffin wax as a result of lower mean stresses in the Vaseline. It is hypothesized that the RCMP is not observed in our experiments due to an impermeable high viscosity matrix.

### 5.3 Strain Localization: Comparison with Previous Work

Numerical modelling conducted by Mancktelow (2001) is directly comparable to our analogue model experiments. Models containing weak inclusions of similar size, distribution, and viscosity contrast are deformed under both pure shear and simple shear boundary conditions in a non-permeable high viscosity matrix. Both pure shear and simple shear boundary conditions produced an anastomosing pattern of shear bands nucleating on weak inclusions. In numerical models using pure shear boundary conditions, each weak inclusion nucleated conjugate shear bands initially at  $90^\circ$  to each other that rotated with progressive deformation. At the resolution of our digital images, we do not observe conjugate shear bands forming at  $45^\circ$  to the bulk compression axis. This can be due to strain partitioning in the analogue models not being strong enough to form shear bands at  $45^\circ$  or because the resolution of the images is not high enough to reveal the first stages of shear band formation. We observe that at approximately 33% shortening, the final number of shear zones is significantly less than the number of weak inclusions in each of the experiments. Since a limited sample size of analogue models is available for analysis, and the distribution of weak inclusions does not follow a pattern, it is not possible to quantitatively analyze the relationship between weak inclusions and the number of shear bands. Our analogue modelling suggests that the relationship is non-linear. At the shortening level which an analogue model first develops a network of shear bands, the number of shear bands is greater in models with a larger number of inclusions. Weak inclusions are found in areas of high strain and areas of low strain. Shear bands localize stress until a high finite strain (not reached in our analogue models) when they have rotated away from the bulk extension axis and do not localize strain any more. Since some weak inclusions are found in areas of low strain, in nature it may therefore appear that there are older more deformed shear zones of leucosomes surrounding younger less deformed leucosomes. Because of strain partitioning, they may be of the same age with a different deformation history.

### 5.5 Shear Band Evolution

Shear band networks appear in the analogue models within the first 12% of

shortening. Except for Run 90, shear band networks formed at later stages with increasing percent volume melt. Shear bands in Run 96 and Run 98 formed within the shortening interval where the stress strain curves of the experiments transition from Regime 3 to Regime to Regime 4 (Figure 15). The shear band network in Run 90 forms when the stress strain curve of the experiment is in Regime 2 (Figure 15). Stress-strain is not available for Run 84 and Run 88. The transition from a linear relationship between stress and strain (Regime 1) and a non-linear relationship (Regime 2) occurs at approximately 1.75% shortening. This transition is thought to correspond to the nucleation of shear bands.

With progressive shortening from amounts below 12% to 19.5%, shear bands become better defined due to an increase in the difference in strain between areas of high strain and low strain. Shear bands became wider and longer at 19.5% shortening. At 32% shortening, each experiment has a well defined pattern of shear bands. As the models are deformed, areas of high strain that are not shear bands evolve into shear bands or are incorporated into existing shear bands.

## 5.6 Deformation

The difference in ratio of stress in the paraffin wax to stress in Vaseline between the experiments is largest at low levels of deformation. The value of  $\Gamma$  ranges between 2 and 22.5 when calculated when shear band networks first develop. Over this interval of  $\Gamma$ , the dimensionless shear band length ratio  $\Lambda$  decreases as a function of  $\Gamma$ . It is unclear whether the data set exhibits a linear or non-linear trend. At 19.5% shortening the range of  $\Gamma$  is reduced to 1.1 to 8.9, and at 32% shortening the range of  $\Gamma$  is further decreased to 0.6 to 5.4. At both these stages of deformation the experimental data suggests that  $\Lambda$  continues to decrease as a function  $\Gamma$  at higher levels of shortening. Because of the variability of measurements of  $\Lambda$  in each experiment at each stage of deformation, the relationship between  $\Gamma$  and  $\Lambda$  is not quantified.

## 5.7 Complications

### 5.7.1 Analogue Materials

The selection of analogue materials used to construct the models was limited by the

capabilities of the deformation rig. Vaseline was selected for the low viscosity inclusions since lower viscosity materials were found to escape the confining plates of the deformation rig in non-negligible amounts. The viscosity of the material used for the high viscosity matrix was limited by the applied differential stress the deformation rig could impose. Analogue materials for this experiment selected accurately reflect the viscosity contrast between natural rocks and partial melt. The use of an impermeable matrix isolated the effects of the viscosity contrast, but does not allow for redistribution of low viscosity materials at low levels of deformation. This mechanism may be necessary to reproduce the RCMP.

#### *5.7.2 Boundary Effects*

Heterogeneous strain in the corners of Run 64 is a result of deviation from pure-shear deformation. These heterogeneities are neither symmetric nor isotropic. Three overlapping plates confine the model in the bulk extension direction and produce irregular stresses at the two discontinuities where the plates overlap. Slight volume loss of paraffin wax at discontinuities between confining and compressing plates in the corners of the analogue models also results in non pure-shear boundary conditions. Vertical bands of higher strain visible in Run 84, Run 88, and Run 90 in Figure 19 are thought to result from boundary effects of the deformation rig.

#### *5.7.3 Inclusion Shape and Distribution*

Vaseline inclusions are distributed approximately randomly in a higher viscosity paraffin wax matrix to form analogue models. The majority of experiments contained cylindrical inclusions with a 5mm diameter. Certain experiments (Table 1) used inclusions that were not cylindrical, or were larger in diameter. Run 92 and Run 84 have equal volume percent melt with inclusions of different size. Stress-strain data for Run 84 are not available and the experiments cannot be compared to investigate the influence of inclusion shape and distribution on bulk rheology.

#### *5.7.4 Experimental Approach*

Experiments are conducted at a constant natural strain rate (Equation 2). At a constant natural strain rate, the engineering strain rate decreases with increasing shortening. Since the rheology of viscous materials is a function of engineering strain-rate history, the rheological properties of the paraffin wax and Vaseline change with progressive deformation. Analytical

and numerical modelling of this style of deformation is difficult because of the evolving rheology of paraffin and Vaseline and because engineering-strain rate is not constant over small finite strains. Deforming the experiments using either a constant applied stress or a constant displacement piston velocity would allow numerical simulations of the evolution of models. (i.e. Butler 2010)

## **6. Conclusion**

The results of analogue model experiments investigating the relationship between partial melt and deformation performed under plain strain, pure shear boundary conditions were analyzed. The presence of partial melt was found to localize strain, and nucleate shear bands. Shear bands connected and formed networks linking low viscosity inclusions in each of the experiments at less than 12% shortening of the experiments. Shear bands became wider and longer with increasing deformation, and the pattern of shear bands evolved with progressive deformation. Flow stress of the analogue models decreased non-linearly with increasing partial melt, though the deviation from a linear relationship was small. No large magnitude decrease in the viscosity of experiments was found over volume percent melt in the range of 20-40% corresponding to the RCMP. Deformation in the experiments was measured using the dimensionless length of shear bands. The dimensionless shear band length was found to decrease as function of the ratio of stress in the high viscosity matrix to the stress in the low viscosity inclusions.

## REFERENCES CITED

- Adam, J., Urai, J. L., Wieneke, B., Oncken, O., Pfeiffer, K., Kukowski, N., Lohrmann, J., Hoth, S., van der Zee, and W., Schmatz, J., 2005, Shear localization and strain distribution during tectonic faulting – new insights from granular-flow experiments and high-resolution optical image correlation techniques, *Journal of Structural Geology*, v. 27, p. 283–301.
- Arzi, Avner A., 1978, Critical phenomena in the rheology of partially melted rock, *Tectonophysics*, v.44, p. 173-184.
- Barraud, J., Gardien, V., Allemand, P., and Grandjean, P., 2001, Analog modelling of melt segregation and migration during deformation, *Physics and Chemistry of the Earth, Part A: Solid Earth and Geodesy*, v. 26, p. 317-323.
- Brown, M., Averkin, Y. A., McLellan, E. L., and Sawyer, E. W., 1995, Melt segregation in migmatites, *Journal of Geophysical Research Solid Earth*, v. 100, p. 655–679.
- Butler, S.L., 2010, Porosity Localizing Instability in a Compacting Porous Layer in a Pure Shear Flow and the Evolution of Porosity Band Wavelength, *Physics of the Earth and Planetary Interiors*, v. 182, p. 30-41.
- Davidson, C., Schmid, S. M. and Hollister, L. S., 1994, Role of melt during deformation in the deep crust, *Terra Nova*, v. 6, p. 133-142.
- Einstein, A., 1906, Eine neue bestimmung der molekuldimensionen, *Annales de Physique*, v. 19, p. 289-306.
- Einstein, A., 1911., Berichtigung zu meiner arbeit: eine neue bestimmung der molekuldimensionen, *Annales de Physique*, v. 34, p. 591-592.
- Grujic, D., and Mancktelow, N. S., 1995, Folds with axes parallel to the extension direction: an experimental study, *Journal of Structural Geology*, v. 17, p. 279-291.
- Grujic, D., and Mancktelow, N.S., 1998, Melt-bearing shear zones: analogue experiments and comparison with examples from southern Madagascar, *Journal of Structural Geology*, v. 20, p. 673-680.
- Handy, Mark R., 1990., The Solid-State Flow of Polymineralic Rocks, *Journal of Geophysical Research*, v. 95, p. 8647-8661.
- Hollister, L. S., and Crawford, M. L., 1986, Melt-enhanced deformation: A major tectonic process, *Geology*, v. 14, p. 558-561.

- Holtzman, B.K., Groebner N.J., Zimmerman M.E., Ginsberg S.B., and Kohlstedt D.L., 2003, Stress-driven melt segregation in partially molten rocks, *Geochemistry Geophysics and Geosystems*, v. 4.
- Holtzman B.K., and Kohlstedt D.L., 2007, Stress-driven melt segregation and strain partitioning in partially molten rocks: Effects of stress and strain, *Journal of Petrology*, v. 48, p. 2379–2406,
- Katz, R. F., Spiegelman, M., and Holtzman, B., 2006, The dynamics of melt and shear localization in partially molten aggregates, *Nature*, v. 442, p. 676-679.
- StrainMaster – Getting Started Manual for DaVis 7.0, 2004, LaVision GmbH.
- Mancktelow, N.S., 1988a, An automated machine for pure shear deformation of analogue materials in plane strain, *Journal of Structural Geology*, v. 10, p. 101-108.
- Mancktelow, N.S., 1988b, The Rheology of paraffin wax and its usefulness as an analogue for rocks, *Bulletin of the Geological Institutions of the University of Uppsala*, v. 14, p. 181–193.
- Mancktelow, N.S., 1991, The analysis of progressive deformation from an inscribed grid, *Journal of Structural Geology*, v. 13, p. 859-864.
- Mancktelow, N.S., 2002, Finite-element modelling of shear zone development in viscoelastic materials and its implications for localization of partial melting, *Journal of Structural Geology*, v. 24, p. 1045-1053.
- Means, W. D., 1995., Shear zones and rock history, *Tectonophysics*, v. 247, p. 157-160.
- Ramsay, J.G., 1980, Shear zone geometry: A review, *Journal of Structural Geology*, v. 2, p. 83-99.
- Ramsay, J.G, and Huber M.I., 1984, *The Techniques of Modern Structural Geology, Volume 1: Strain Analyses*, Academic Press.
- Roscoe, R., 1952, The viscosity of suspensions of rigid spheres, *British Journal of Applied Physics*, v. 3, p. 267-269.
- Rosenberg, C. L., and Handy, M. R., 2000, Syntectonic melt pathways during simple shearing of a partially molten rock analogue (Norcamphor-Benzamide), *Journal of Geophysical Research*, v. 105, p. 3135–3149.
- Rosenberg, C. L., and Handy, M. R., 2005, Experimental deformation of partially melted granite revisited: implications for the continental crust, *Journal of Metamorphic Geology*, v. 23, p. 19-28.

- Rushmer, T., 1995, An experimental deformation study of partially molten amphibolite: Application to low-melt fraction segregation, *Journal of Geophysical Research*, v. 100, p. 681–695.
- Rutter, E.H., and Neumann, D.H.K., 1995, Experimental deformation of partially molten Westerly granite under fluid-absent conditions, with implications for the extraction of granitic magmas, *Journal of Geophysical Research*, v. 100, p. 697-715.
- Rutter, E.H., Brodie, K. H., and Irving, D.H., 2006, Flow of synthetic, wet, partially molten “granite” under undrained conditions: An experimental study, *Journal of Geophysical Research*, v. 111.
- Spiegelman, M, 1993, Flow in Deformable Porous Media. Part 1 Simple Analysis, *Journal of Fluid Mechanics*, v. 247, p. 17-38.
- Spiegelman, M. 2003. Linear analysis of melt band formation by simple shear, *Geochemistry Geophysics and Geosystems*, v. 4.
- Stevenson, D. J., 1989, Spontaneous small-scale melt segregation in partial melts undergoing deformation, *Geophysical Research Letters.*, v. 16, p. 1067–1070.
- Takeda, YT, and Masaaki O., 2003, Some comments on the rheologically critical melt percentage, *Journal of Structural Geology*, v. 25, p. 813-818.
- Twiss and Moores, 2007. *Structural Geology*, 2<sup>nd</sup> Edition. New York, NY. W.H Freeman and Company.
- van der Molen, I., and Paterson M.S., 1979, Experimental deformation of partially-melted granite, *Contributions to Mineralogy and Petrology*, v. 70, p. 299-318.
- Vigneresse, J.L., Barbey, P., and Cuney. M., 1996, Rheological Transitions during partial melting and crystallization with application to felsic magma segregation and transfer, *Journal of Petrology*, v. 37, p. 1579-1600.